

# Hydroclimatic anomalies detected by a sub-decadal diatom oxygen isotope record of the last 220 years from Lake Khamra, Siberia

5 Amelie Stieg<sup>1,2</sup>, Boris K. Biskaborn<sup>1</sup>, Ulrike Herzschuh<sup>1,2,3</sup>, Jens Strauss<sup>1</sup>, Luidmila Pestryakova<sup>4</sup>, Hanno Meyer<sup>1</sup>

<sup>1</sup>Alfred Wegener Institute Helmholtz Centre for Polar and Marine Research, Potsdam, 14473, Germany.

<sup>2</sup>Institute of Environmental Science and Geography, University of Potsdam, Potsdam, 14476, Germany.

10 <sup>3</sup>Institute of Biochemistry and Biology, University of Potsdam, Potsdam, 14476, Germany.

<sup>4</sup>Institute of Natural Sciences, North-Eastern Federal University of Yakutsk, Yakutsk, 677007, Russia.

Correspondence to: Amelie Stieg (amelie.stieg@awi.de)

15 **Abstract.** Northern latitudes have been significantly impacted by recent climate warming, which has increased  
the probability of experiencing extreme weather events. To comprehensively understand hydroclimate change and  
reconstruct hydroclimatic anomalies such as drought periods, appropriate proxy records reaching further back in  
time are needed beyond meteorological measurements. Here we present a 220-year (2015–1790CE), continuous  
stable oxygen isotope record of diatoms ( $\delta^{18}\text{O}_{\text{diatom}}$ ) from Lake Khamra (59.99° N, 112.98° E) in Eastern Siberia,  
20 an area highly sensitive to climate change and with a demand for palaeohydrological data. From a  $^{210}\text{Pb}$ - $^{137}\text{Cs}$ -  
dated sediment short core, this high-resolution proxy record was analysed to reconstruct hydroclimate variability  
on a sub-decadal scale. The interpretation of the  $\delta^{18}\text{O}_{\text{diatom}}$  is supported by meteorological data, modern isotope  
hydrology and geochemical analyses of the same sediment indicative for the conditions in lake and catchment. A  
comparison with meteorological data back to 1930CE revealed that the  $\delta^{18}\text{O}_{\text{diatom}}$  record of Lake Khamra is  
25 primarily influenced by regional precipitation changes rather than air temperature. We identified winter  
precipitation, which enters the lake as isotopically-depleted snowmelt water, as the key process impacting the  
diatom isotope variability. We related the overall depletion of  $\delta^{18}\text{O}_{\text{diatom}}$  in recent decades to an observed increase  
in winter precipitation in the area, likely associated with the global air temperature rise, Arctic sea ice retreat and  
increased moisture transport inland. Available palaeoclimate proxy records, including a fire reconstruction of the  
30 same lake, support the new record as a valuable hydroclimate proxy indicative for precipitation deficits,  
tendentially excluding solar insolation and air temperature as driving forces even beyond meteorological  
recordings. We propose two possible hydroclimatic anomalies detected in the Lake Khamra  $\delta^{18}\text{O}_{\text{diatom}}$  record: one  
at the beginning of the 19<sup>th</sup> century and a second prominent event in the 1950s. Both are interpreted as prolonged  
dry periods, associated with enriched  $\delta^{18}\text{O}_{\text{diatom}}$  values likely caused by reduced winter precipitation, which  
35 coincide with phases of reconstructed severe wildfires in the region. Despite the apparent pristine lake area, we  
observed a three- to fourfold increase of mercury concentrations and accumulation rates within the sediment record  
since the early 20<sup>th</sup> century, partly attributed to human air pollution.

## 1 Introduction

Siberia experienced an extraordinary heatwave during the initial six months of 2020 (Overland and Wang, 2020; Collow et al., 2022), highly improbable without human-induced climate change (Ciavarella et al., 2021). Since 1979, the northern latitudes have warmed nearly four times faster than the rest of the world (Rantanen et al., 2022) and this warming has even accelerated since the beginning of the 21<sup>st</sup> century (Chylek et al., 2022), a phenomenon known as Arctic Amplification (Manabe and Stouffer, 1980; Miller et al., 2010; Previdi et al., 2021). Rapidly increasing air temperatures due to rising emissions of greenhouse gases result in higher frequency and/or intensity of extreme events (Seneviratne et al., 2021). Hydroclimate extreme events, such as drought periods or intensified precipitation, are linked with ocean currents and large-scale dynamics (Churakova Sidorova et al., 2021; Marshall, 2021; Seneviratne et al., 2021; Watanabe et al., 2023). In the 21<sup>st</sup> century, Arctic precipitation is expected to increase significantly due to Arctic sea-ice retreat and increased evaporation (Bintanja and Selten, 2014; Bintanja, 2018).

The hydroclimate across Siberia has undergone notable alterations in recent decades, but differs regionally. While snow depth decreased over most southern parts of Russia, it increased in the northern parts including northern central Siberia (Ye et al., 1998; Bulygina et al., 2009; Ghatak et al., 2012; Sato et al., 2022). In Yakutia, the Republic of Sakha, located in the Russian Far East (Fig. 1a), the snow cover duration was prolonged (Bulygina et al., 2009) and in the past five decades, there has been a notable rise in overall precipitation levels (Gorokhov and Fedorov, 2018). Despite this, Yakutia is one of the most vulnerable regions for forest fires in Russia (Kirillina et al., 2020) and underwent its most severe fire season of the past forty years in 2021 (Tomshin and Solovyev, 2022), highlighting an area of extremes. Meteorological records only start in the beginning of the 20<sup>th</sup> century, and there is a scarcity of high-resolution hydroclimate records predating this period.

To reconstruct hydroclimatic anomalies, appropriate high-resolution proxy records are needed. Oxygen isotopes of lacustrine diatoms ( $\delta^{18}\text{O}_{\text{diatom}}$ ) have proven to be a valuable proxy to investigate temperature and hydrological variations in numerous studies (Leng and Barker, 2006; van Hardenbroek et al., 2018).  $\delta^{18}\text{O}_{\text{diatom}}$  is influenced by different environmental and climatic factors, such as precipitation, evaporation or atmospheric circulation patterns, and is generally linked to variations in temperature and the oxygen isotope composition of the lake water ( $\delta^{18}\text{O}_{\text{lake}}$ ; Leng and Barker, 2006; Meister et al., 2023). Nevertheless, influencing factors vary by location and have to be evaluated for each study site individually. Diatom oxygen isotope records located in Russia have been interpreted as a palaeo-precipitation proxy (Chapligin et al., 2012b; Kostrova et al., 2013a; 2013b; Meyer et al., 2022), or a proxy sensitive to snow or glacier meltwater input (Mackay et al., 2013; Kostrova et al., 2013b, 2014; Meyer et al., 2015; Kostrova et al., 2021; Meyer et al., 2022), dominated by summer temperatures on millennial timescales (Meyer et al., 2022). Furthermore, long-term trends in the  $\delta^{18}\text{O}_{\text{diatom}}$  records correspond to those in summer insolation (Meyer et al., 2015; Kostrova et al., 2021; Meister et al., 2023) and teleconnections between Central Asia and the North Atlantic could be identified (Mackay et al., 2013). The available lake sediment  $\delta^{18}\text{O}_{\text{diatom}}$  records predominantly cover the Holocene, and especially the last two thousand years (Meister et al., 2023). For Asia, there are 21 diatom isotope records published, with special emphasis on Siberia (Meister et al., 2023). However, the  $\delta^{18}\text{O}_{\text{diatom}}$  records mainly focus on millennial time scales whereas high-resolution records of the past hundred years are very scarce. Moreover, there is only one Russian high-resolution study at Lake Baikal interpreted as a hydroclimate proxy (Swann et al., 2018; cf. Fig. 1a).

This study aims to provide a new hydroclimate proxy record from Lake Khamra (59.99° N, 112.98° E) in Southern Yakutia (Fig. 1a). We hypothesise that a high-resolution  $\delta^{18}\text{O}_{\text{diatom}}$  record can be used to reconstruct hydroclimatic

anomalies on a sub-decadal scale, such as drought events or prolonged rainfall periods since 1790CE. For this  
80 purpose, the latest 90 years of the record are validated by meteorological data to identify main drivers of the  
 $\delta^{18}\text{O}_{\text{diatom}}$  record in the study area. Comparison with available palaeoclimate proxy records are used to assess key  
factors responsible for the diatom isotope variability and to analyse common trends beyond meteorological time  
scales. For the identification of large-scale dynamics, the  $\delta^{18}\text{O}_{\text{diatom}}$  record is placed in the broader context of the  
northern landscape development. Additionally, we survey a possible human impact on this remote lake ecosystem  
85 since the onset of the industrial revolution.

## 2 Study area and regional climate

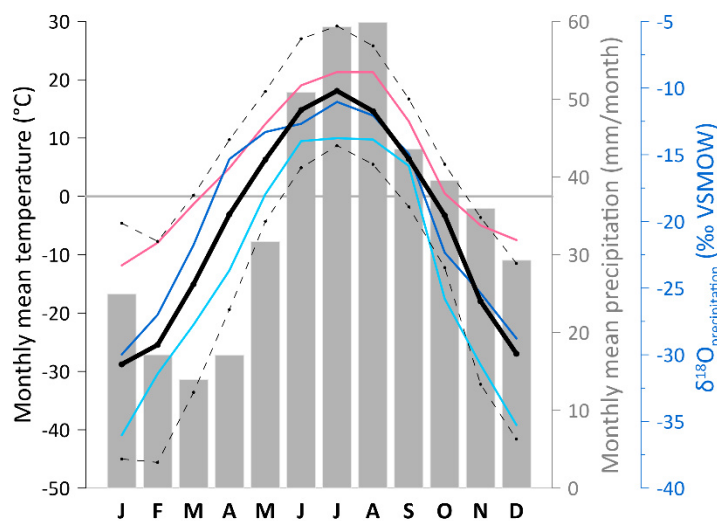


90 **Figure 1. Study area. a)** Position of Lake Khamra in the south-western part of Yakutia, close to the Lena river; closest weather station is located in Vitim, Lake Khamra lies in between the cities Yakutsk and Irkutsk. Other high-resolution study sites are indicated as grey triangles (Jonsson et al., 2010; Swann et al., 2018; Broadman et al., 2022). **b)** Catchment of Lake Khamra, main in- and outflow are indicated by arrows. **c)** Sample locations at Lake Khamra. (Service layer credits: © OpenStreetMap contributors 2023. Distributed under the Open Data Commons Open Database License (ODbL) v1.0.; Esri, Maxar, Earthstar Geographics, and the GIS User Community).

95 Lake Khamra (59.99° N, 112.98° E, 340 m a.s.l.) is located in Eastern Siberia, in a sparsely populated area in south-west Yakutia, Russia (Fig. 1a). The closest urban settlements, Peleduy and Vitim, are situated 40 and 60 km south-west of the lake, respectively. The city of Yakutsk is located 930 km to the north-east, Irkutsk ca. 1000 km to the south-west.

Lake Khamra covers an area of 4.6 km<sup>2</sup> and has a catchment size of 107.3 km<sup>2</sup>, extending towards the south-west.  
 100 The water depth ranges from shallow shore areas towards a maximum of 22.3 m in the central part of the lake (Fig. 1c). There are several small tributaries flowing down the gentle hills into the lake, with the main inflow to the south-west and an outflow in the north-east (Fig. 1b). The lake is a hydrologically open system with an estimated average long-term discharge of 1.1 m<sup>3</sup> s<sup>-1</sup> (0.03 km<sup>3</sup> a<sup>-1</sup>) and an average residence time of approximately 474 days (Messenger et al., 2016). In winter, the lake is covered by ice and snow. During field work in March 2020, the ice  
 105 thickness was on average 0.5 m and the snow cover was about 1 m thick at different drilling locations (Biskaborn et al., 2021a).

The lake is located within Cambrian bedrock comprising dolomite and limestone alternating with silty Ordovician sandstone and small delineated areas of clayey Silurian limestone (Chelnokova et al., 1988). The landscape is classified as mountain taiga within a discontinuous and sporadic permafrost zone (Brown et al., 1997; Fedorov et al., 2018). According to field observations, the catchment of the mountain lake Khamra is covered by a mixed-  
 110 coniferous forest, mainly consisting of the tree species *Larix gmelinii*, *Picea obovata*, *Pinus siberica* and *Abies siberica* (Kruse et al., 2019; Miesner et al., 2022).



115 **Figure 2. Meteorological data from the weather station Vitim (59.45° N, 112.58° E, 186 m a.s.l., ECA station code 3235), data accessible via the KNMI Climate Explorer <https://climexp.knmi.nl>: monthly mean precipitation amount 1929–2018CE, 90 yrs. (grey bars) and monthly mean temperature 1929–2018CE, 90 yrs. (black line; Klein Tank et al., 2002); daily max temperature 1930–2019CE (upper dashed line) and min temperature 1928–2019CE (lower dashed line, Durre et al. 2008). Monthly mean oxygen isotope values of precipitation (δ<sup>18</sup>O<sub>prec</sub>) recorded in Yakutsk is shown by the light blue line (Kurita et al., 2004), recorded in Irkutsk is highlighted by the dark blue line (Kostrova et al., 2020). Modelled monthly δ<sup>18</sup>O<sub>prec</sub> values for the region (latitude 60°, longitude 113°, altitude 340 m) is shown as pink line (Bowen et al., 2005; Bowen, 2023; IAEA/WMO, 2023).**  
 120

According to the nearest weather station in Vitim (Fig. 1a) the region of Lake Khamra is strongly influenced by  
 125 the continental climate, characterised by a large annual temperature range of 47°C from extremely cold and dry winters (lowest monthly mean temperature in January: -28.8°C, 1929–2018CE) to warm and humid summer

months (highest monthly mean temperature July: +18.1°C, 1929–2018CE). The mean annual air temperature is -5.0°C with an annual mean precipitation amount of 423 mm (1929–2018CE), with most precipitation falling between June and September (cf. Fig. 2). The variability of snow accumulation in the area may depend on changing air-mass trajectories and changing moisture sources. Between November and March, the Siberian high is predominant as a shallow high-pressure system above Central Siberia, associated with very cold and dry conditions (Shahgedanova, 2002). Winter precipitation is linked with frontal activity and mainly influenced by the Icelandic Low in the northwest and the Aleutian Low in the northeast linked to a depression in the upper troposphere (Mock et al., 1998; Shahgedanova, 2002). Thereby, moisture is generally transported from the Icelandic Low originating from the North Atlantic by westerly winds to Central Siberia (Shahgedanova, 2002). Oxygen isotope measurements of precipitation ( $\delta^{18}\text{O}_{\text{prec}}$ ), recorded in Yakutsk (Kurita et al., 2004) and Irkutsk (Kostrova et al., 2020), as well as the modelled monthly  $\delta^{18}\text{O}_{\text{prec}}$  values for the region (Bowen et al., 2005; Bowen, 2023; IAEA/WMO, 2023) all follow the annual pattern of the temperature amplitude, with strongly depleted values in the winter months and more enriched values in summer (cf. Fig. 2). Overall, the modelled data shows the highest  $\delta^{18}\text{O}_{\text{prec}}$  values, the Yakutsk region the lowest.

### 3 Methods

#### 3.1 Water isotope samples of Lake Khamra and meteorological data

During two field campaigns, in August 2018 and in March 2020, the isotopic composition of the lake water was analysed. During the summer field campaign in 2018, surface water (0–0.05 m) was sampled in the central part of the lake and hydrological parameters like pH, conductivity and temperature were measured on site using a WTW Multilab 340i. In spring 2020, six water samples along a water-depth profile were taken, below a lake ice cover of 0.65 m, which was additionally sampled. Two snow samples were collected near the shore within a profile of 60 cm (see map for the different sample locations, Fig. 1c).

The snow and ice samples were all completely melted and subsequently stored cool in 30 ml PE-bottles prior to stable isotope measurements. Hydrogen ( $\delta\text{D}$ ) and oxygen ( $\delta^{18}\text{O}$ ) isotopes were analysed at the ISOLAB Facility at the Alfred Wegener Institute Helmholtz Centre for Polar and Marine Research (AWI) in Potsdam, Germany, with a Finnigan MAT Delta-S mass spectrometer employing the equilibration method (details in Meyer et al. 2000). Data are given in per mil (‰) relative to Vienna Standard Mean Ocean Water (V-SMOW). The standard deviation includes all measurements of the individual sample, which is generally better than the external (or machine) error. The external errors of long-term standard measurements for hydrogen and oxygen are better than  $\pm 0.8\text{‰}$  and  $\pm 0.10\text{‰}$ , respectively (Meyer et al., 2000). The second order parameter deuterium excess (d excess) was computed according to:  $d = \delta\text{D} - 8 * \delta^{18}\text{O}$  (Dansgaard, 1964).

The water isotope samples of Lake Khamra are compared to the Global Meteoric Water Line (GMWL):  $\delta\text{D} = 8 * \delta^{18}\text{O} + 10$  (Craig, 1961) and to Global Network for Isotopes in Precipitation (GNIP) data (IAEA/WMO, 2023) recorded in Yakutsk (Kurita et al., 2004) and in Irkutsk (Kostrova et al., 2020). Additionally, the mean monthly and annual isotope composition of precipitation were modelled for the study area (latitude 60°, longitude 113°, altitude 340 m) using the Online Isotopes in Precipitation Calculator (OIPC; Bowen and Revenaugh, 2003; Bowen et al., 2005; Bowen, 2023; IAEA/WMO, 2023). The monthly modelled data serves as basis for the Local Meteoric Water Line (LMWL).

All meteorological data used in this study stems from the KNMI Climate Explorer website (<https://climexp.knmi.nl>), from the weather stations in Vitim (59.45° N, 112.58° E, 186 m a.s.l., ECA station code 3235, 1928–2019CE), Yakutsk (62.02° N, 129.72° E, 98 m a.s.l., ECA station code: 3214, 1888–2019CE) and Irkutsk (52.27° N, 104.35° E, 467 m a.s.l., ECA station code: 3245; 1882–2018CE; Klein Tank et al., 2002). For comparability with the weather station in Vitim, only meteorological data for the years 1929–2018CE were considered.

### 3.2 Sediment short core recovery and subsampling

During the field work in August 2018, a 42 cm sediment short core, EN18232-1, was retrieved from the central and deepest part of Lake Khamra (59.99091° N; 112.98373° E; water depth: 22.3 m) by using an UWITEC gravity corer (60 mm). The water depth was determined with a surveying rope and a handheld HONDEX PS-7 LCD digital sounder. After the field work, the sediment core was transported in a PVC tube to the AWI in Potsdam and stored dark and cool at 4°C until further analysis.

In October 2021, the short core was subsampled gapless in 1 cm increments (n=39). The rim material (<0.5 cm) of the individual sample layers was removed to avoid contamination. With the help of a 1 cm<sup>3</sup> tool, additionally 24 subsamples were taken to determine the water content and dry bulk density (0–10 cm every 1 cm; >10 cm every 2 cm). All sediment samples were frozen and subsequently freeze dried for at least 48 h.

### 3.3 Dating

For establishing the high-resolution age-depth model, freeze-dried subsamples of the short core EN18232-1 (n=31) were analysed for <sup>210</sup>Pb, <sup>226</sup>Ra, <sup>137</sup>Cs and <sup>241</sup>Am by direct gamma assay in the Liverpool University Environmental Radioactivity Laboratory, using Ortec HPGe GWL series well-type coaxial low background intrinsic germanium detectors (Appleby et al., 1986).

With the intention of extending the <sup>210</sup>Pb–<sup>137</sup>Cs age-depth model, subsamples (n=4) of the freeze-dried bulk material of the deeper part of the short core were sent to the radiocarbon analysis laboratory at AWI Bremerhaven. No plant macrofossils were found in the very fine-grained sample material and thus only bulk sediment samples were dated. <sup>14</sup>C was analysed by using an accelerator mass spectrometer (AMS) MICADAS (Mini Carbon Dating System; Mollenhauer et al., 2021) and calibrated with the IntCal20 <sup>14</sup>C calibration curve (Reimer et al., 2020), using the CALIB Radiocarbon Calibration Program (CALIB REV 8.2; Stuiver and Reimer, 1986, 1993).

To compute the age-depth model a Bayesian accumulation model within the R package ‘rbacon’ v2.5.8 (Blaauw and Christen (2011); R version 4.1.1) was used based on the <sup>210</sup>Pb chronology.

### 3.4 Diatom isotope purification process, $\delta^{18}\text{O}_{\text{diatom}}$ analysis and contamination correction

The diatom isotope purification process includes both chemical and physical preparation steps to obtain a purified diatom sample (Morley et al., 2004; Leng and Barker, 2006). 2 g aliquots of dried sediment samples (n=39) were processed for  $\delta^{18}\text{O}_{\text{diatom}}$  analysis. The cleaning procedure is based on the processing steps described in Morley et al. (2004) and refined in Kostrova et al. (2021). However, processing depends on the respective material and requires an individual approach (Leng and Sloane, 2008). Relevant steps include the removal of organic matter by



adding H<sub>2</sub>O<sub>2</sub> (30%, 50°C, ~55 h), followed by HCl (10%, 50°C, ~16 h) to eliminate carbonates. Before starting  
 205 the heavy liquid separations (HLS), all samples were washed neutrally with ultra-pure water. By centrifuging the  
 samples in sodium polytungstate solutions (SPT, 3Na<sub>2</sub>WO<sub>4</sub>·9H<sub>2</sub>O) with decreasing densities (2.50–2.12 g  
 cm<sup>-3</sup>), the diatoms were gradually separated from the heavy minerogenic fraction. An inverse HLS, described in  
 detail in Kostrova et al. (2021), detached light micro-particles like charcoal from the diatom valves. To remove  
 possible residues of acid, SPT and clay minerals, all samples were washed neutrally with ultra-pure water using a  
 210 3 µm cellulose filter.

Contamination assessment of all processed samples (n=39), was carried out by a JEOL M-IT500HR analytical  
 scanning electron microscope (SEM) with an integrated Energy-Dispersive X-ray Spectroscopy (EDS) system  
 supplied with a Peltier element cooled SD detector (SDD). The standardless procedure was used according to  
 Chaplignin et al. (2012a) (six repetitions, acceleration voltage of 20.0 kV, magnification of 300, measuring time of  
 215 30 seconds). Detected elements are given as oxides with weight percentages. The SiO<sub>2</sub> content indicates the purity  
 of the processed sample, whereas Al<sub>2</sub>O<sub>3</sub> is used as an indicator of contamination with clay fractions. The latter  
 should be below 2.5% to avoid excessive shifts in the δ<sup>18</sup>O<sub>diatom</sub> record due to the contamination correction  
 (Chaplignin et al., 2012a). All 39 samples were highly purified for δ<sup>18</sup>O measurements, with an Al<sub>2</sub>O<sub>3</sub> content  
 ranging between 0.4 and 0.7% and with a SiO<sub>2</sub> content of 96.1 to 98.7%. EDS results, including the two oxides,  
 220 are given in the appendices (Table A1).

Before isotope measurement, aliquots of the processed sample material were heated up at 1100°C by ramp  
 degassing under a Helium flow to remove the exchangeable hydroxyl groups of the siliceous diatom cell walls  
 applying the inert Gas Flow Dehydration method (iGFD; Chaplignin et al., 2010). The oxygen isotope composition  
 of the samples (n=39; contaminants, n=3) was measured at the ISOLAB Facility at AWI Potsdam with a semi-  
 225 automated laser-fluorination line (Chaplignin et al., 2010) combined with a SERCON HS2022 mass spectrometer.  
 The laser fluorination method uses bromine pentafluoride (BrF<sub>5</sub>) as a reagent to completely release oxygen  
 (Clayton and Mayeda, 1963).

The oxygen isotope composition was directly measured against reference material of known isotopic composition,  
 given as delta notation (δ<sup>18</sup>O) relative to VSMOW in per mil (‰). We used the laboratory standards PS Jun17  
 230 (δ<sup>18</sup>O = +43.61‰ ± 0.16‰, n=13), calibrated against the marine standard PS1772-8 (Chaplignin et al., 2010; 2011),  
 and BFC 1 (δ<sup>18</sup>O = +28.92‰ ± 0.08‰, n= 19), calibrated against the standard biogenic silica (BFC; Chaplignin et  
 al., 2011). All samples were measured twice, partly three times. Analytical reproducibility of the sample material  
 was ≤ 0.26‰, indicating an accuracy and analytical precision comparable to the method's long-term analytical  
 reproducibility (1σ) of ± 0.25‰ (Chaplignin et al., 2010).

235 All δ<sup>18</sup>O measurements (δ<sup>18</sup>O<sub>meas</sub>) were contamination corrected (δ<sup>18</sup>O<sub>corr</sub>) following a geochemical mass-balance  
 approach (Brewer et al., 2008; Swann and Leng, 2009; Chaplignin et al., 2012a):

$$\delta^{18}\text{O}_{\text{corr}} = \left( \delta^{18}\text{O}_{\text{meas}} - \frac{c_{\text{cont}} * \delta^{18}\text{O}_{\text{cont}}}{100} \right) / \left( \frac{c_{\text{diatom}}}{100} \right), \quad (1)$$

where δ<sup>18</sup>O<sub>cont</sub> represents the average δ<sup>18</sup>O value of three samples of the heavy minerogenic fraction from the first  
 240 heavy liquid separation of >2.50 g cm<sup>-3</sup> (δ<sup>18</sup>O<sub>cont</sub> = +16.1 ± 0.40‰, n=3), assumed as 100% of contamination. The  
 percentages of contamination (c<sub>cont</sub>) is based on the individual Al<sub>2</sub>O<sub>3</sub> content of each sample divided by the mean  
 Al<sub>2</sub>O<sub>3</sub> content of the contaminants (11.3 ± 0.39% Al<sub>2</sub>O<sub>3</sub>, n=3) using the EDS results, where c<sub>diatom</sub> gives the degree  
 of purity (100% - c<sub>cont</sub>).

In order to increase comparability and to detect the impact of hydroclimate variability within the  $\delta^{18}\text{O}_{\text{diatom}}$  record, the isotope values were standardised. Therefore, z-scores of each  $\delta^{18}\text{O}_{\text{diatom}}$  value were calculated by subtracting the overall mean and dividing it by the standard deviation of the time series.

### 3.5 Further lake internal proxies

The inorganic carbon (TIC) content was determined of all 39 subsamples, to analyse it as a possible proxy for sediment supply from the carbonate-bearing bedrock in the catchment, as outlined in Lenz et al. (2021). Prior to measurements, freeze-dried aliquots were milled to gain a homogeneous material. TIC was measured by using an Elementar soli TOC cube. The measurement accuracy was  $\pm 0.1\%$ . To detect possible heavy metal pollution within the sediment record, total mercury concentrations (THg) were quantified in all subsamples. THg was measured with a MLS-MWS DMA-80 evo III at the Permafrost Carbon and Nitrogen Lab (CarLa) at AWI Potsdam, given in  $\mu\text{g kg}^{-1}$ . The machine detection limit was 0.003 ng, with a laboratory proven limit of determination of 0.4 ng. Furthermore, mercury concentrations were converted into fluxes (HgAR,  $\mu\text{g m}^{-2} \text{a}^{-1}$ ) following the procedure described in detail in Biskaborn et al. (2023). The sedimentation rates (SR in  $\text{cm a}^{-1}$ ) were calculated using the age-depth-model results according to Eq. (2) (Pfalz et al., 2022), whereby  $xi$  is the sample depth of interest and  $xi-1$  its previous layer:

$$SR_{(xi)} = \frac{\text{depth}_{(xi)} - \text{depth}_{(xi-1)}}{\text{age}_{(xi)} - \text{age}_{(xi-1)}}, \quad (2)$$

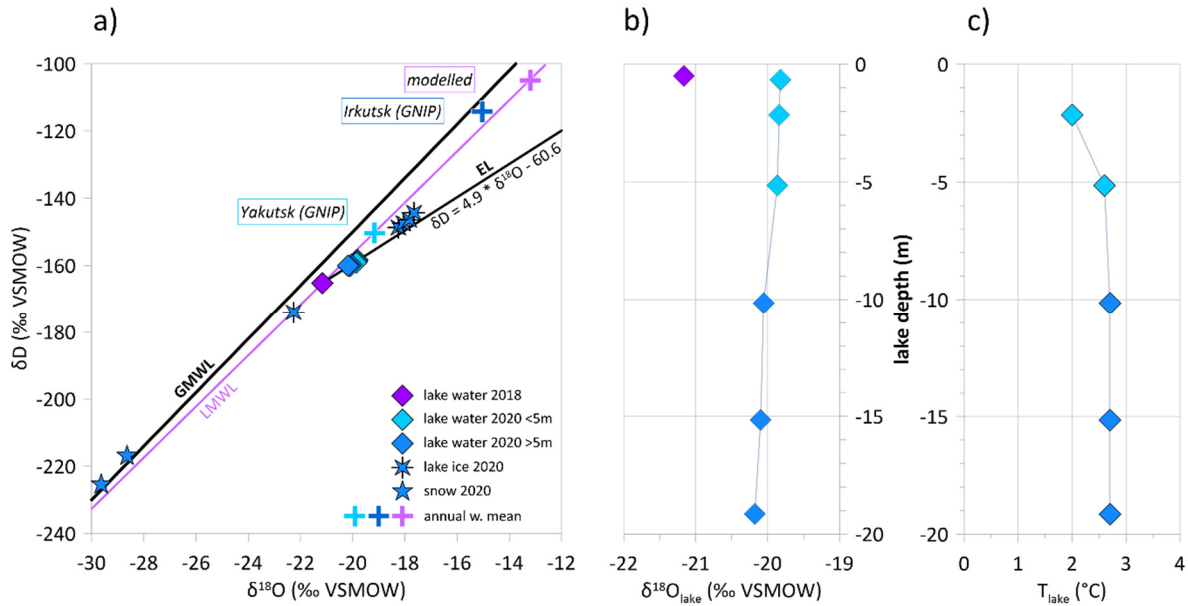
Subsequently, the mass accumulation rate (MAR in  $\text{g cm}^{-2} \text{a}^{-1}$ ) were computed by using following equation (Eq. (3)), where DBD is the dry bulk density (in  $\text{g cm}^{-3}$ ). We used the mean dry bulk density value here:

$$MAR = DBD * SR, \quad (3)$$

to consequently calculate the mercury accumulation rates HgAR in  $\mu\text{g m}^{-2} \text{a}^{-1}$ :

$$HgAR = Hg * MAR * 10 \quad (4)$$

## 4.1 Water isotopes of Lake Khamra



275 **Figure 3. a)** Co-Isotope plot ( $\delta^{18}O$ - $\delta D$ ) of lake water, ice and snow samples taken during the two field campaigns in August 2018 and March 2020, in relation to the GMWL (Craig, 1961) and the LMWL according to the modelled monthly mean values. Annual weighted mean values of precipitation modelled for the region (Bowen and Revenaugh, 2003; Bowen et al., 2005; Bowen, 2023; IAEA/WMO, 2023) and from the GNIP stations in Yakutsk and Irkutsk (IAEA/WMO, 2023) are marked as crosses. The intercept point of the local evaporation line (EL) and modelled LMWL is at  $\delta^{18}O$  -20.9‰ and  $\delta D$  -164.0‰. **b)**  $\delta^{18}O$  of a water-depth profile of Lake Khamra, sampled below lake ice in March 2020 **c)**  $T_{lake}$  of the water-depth profile, taken below ice cover in March 2020.

280

Water, ice and snow isotope data sampled during the two field campaigns are shown in a  $\delta^{18}O$ - $\delta D$  diagram (Fig. 3a). According to the surface water sample collected in summer 2018,  $\delta^{18}O_{lake}$  has a value of -21.16‰,  $\delta D_{lake}$  of -165.3‰ and a d excess of +4.1‰ (n=1). The water sample has a pH of 6.07. In March 2020,  $\delta^{18}O_{lake}$  had a mean of -19.98‰  $\pm$  0.14‰,  $\delta D_{lake}$  of -159.3‰  $\pm$  0.7‰ and a d excess of +0.5‰  $\pm$  0.5‰ (n=6), which is isotopically 285 enriched in comparison to the isotope values of 2018.  $\delta^{18}O_{lake}$  reveals only small variations of  $\pm$ 0.35‰ within the water profile with continuously depleted towards the bottom water (see Fig. 3b). The lake water temperature ( $T_{lake}$ ) below the ice cover is quite low, varying from a minimum of 2°C to 2.7°C downwards (Fig. 3c). All measurements are listed in Table 1.

The ice cover of the lake, with a total thickness of 0.68 m, was sampled in 5 segments in March 2020 (see Table 290 1). The  $\delta^{18}O$  values vary by  $\pm$ 4.6‰, with a minimum of -22.3‰ at the surface and a maximum of -17.7‰ at the transition from ice to water.  $\delta D$  ranges from -174.1‰ at the top to -144.3‰ at the bottom. This results in a positive d excess value of +4.0‰ in the upper ice sample and negative d excess values in the lower samples, down to -3.8‰. The snow samples, collected close to the lakeshore, reveal the lowest  $\delta^{18}O$  values with a mean of -29.14‰ and  $\delta D$  of -221.2‰, respectively, and a d excess of +11.9‰. In comparison to the GMWL (Craig, 1961), only the 295 snow samples lie slightly above the GMWL, all water and ice samples of Lake Khamra lie slightly below the GMWL, and below or along the modelled LMWL of monthly values (Fig. 3a; Bowen et al., 2005; Bowen, 2023; IAEA/WMO, 2023). The modelled annual mean for the region ( $\delta^{18}O$ : -13.2‰,  $\delta D$ : -105‰, Bowen and Revenaugh, 2003; Bowen, 2023; IAEA/WMO, 2023) is offset from the measurement results towards more enriched values (Fig. 3a).

**Table 1. Water, ice and snow samples from Lake Khamra, received in August 2018 and March 2020. The water temperature, measured in August 2018CE, is probably incorrect and not further used for interpretation. Conductivity of water sample EN18232 is given in  $\mu\text{S cm}^{-1}$ , conductivity of the water samples collected in March 2020 measured in  $\text{mg L}^{-1}$ .**

Sample ID	Sample type	Sampling date	Sampling depth top (m)	Sampling depth bottom (m)	Lake Ice thickness (m)	$\delta^{18}\text{O H}_2\text{O}$ (% VSMOW)	1 std dv	$\delta\text{D H}_2\text{O}$ (% VSMOW)	1 std dv	d excess (‰)	N	Temperature ( $^{\circ}\text{C}$ )	Conductivity ( $\mu\text{S cm}^{-1}$ , $\text{mg L}^{-1}$ )
EN18232	water	2018-08-14	0.0	0.05	0	-21.16	0.03	-165.3	0.2	4.1	1	(21.7)	40
EN20001-01/0-5	water	2020-03-10	0.0	0.5	0.65	-19.82	0.02	-158.3	0.3	0.3	1		58
EN20001-01/1,5-2	water	2020-03-10	1.5	2.0	0.65	-19.84	0.01	-158.8	0.2	0.0	1	2.0	42
EN20001-01/4,5-5	water	2020-03-10	4.5	5.0	0.65	-19.87	0.03	-159.1	0.4	-0.2	1	2.6	45
EN20001-01/9,5-10	water	2020-03-10	9.5	10.0	0.65	-20.06	0.02	-159.8	0.4	0.7	1	2.7	50
EN20001-01/14,5-15	water	2020-03-10	14.5	15.0	0.65	-20.10	0.02	-160.1	0.4	0.6	1	2.7	53
EN20001-01/18,5-19	water	2020-03-10	18.5	19.0	0.65	-20.18	0.04	-160.0	0.3	1.4	1	2.7	61
EN20015/0-4/IceCore	ice core	2020-03-17	0.00	0.04	0.68	-22.27	0.10	-174.1	1.2	4.0	3		
EN20015/4-20/IceCore	ice core	2020-03-17	0.04	0.20	0.68	-18.25	0.15	-148.7	0.8	-2.7	3		
EN20015/20-36/IceCore	ice core	2020-03-17	0.20	0.36	0.68	-18.06	0.14	-147.4	0.4	-2.9	3		
EN20015/36-52/IceCore	ice core	2020-03-17	0.36	0.52	0.68	-17.83	0.21	-146.4	1.1	-3.8	2		
EN20015/52-68/IceCore	ice core	2020-03-17	0.52	0.68	0.68	-17.65	0.00	-144.3	0.0	-3.1	2		
EN20016/0-30/Snow	snow	2020-03-17	0.00	0.30		-28.64	0.11	-217.0	0.4	12.2	2		
EN20016/30-60/Snow	snow	2020-03-17	0.30	0.60		-29.63	0.16	-225.4	2.4	11.7	2		

305

## 4.2 Age-depth model

The sample material appeared very uniform in colour during sampling without visible stratifications. The dry bulk density of the short core EN18232-1 is variable likely a result of the high and fluctuating water content (82–94%,  $n=24$ ), especially in the upper part of the short core. Therefore, we determined a mean dry bulk density (122  $\pm$ 35  $\text{mg cm}^{-3}$ ,  $n=38$ ). The homogeneity of the sample material is visible in the results of the  $^{210}\text{Pb}$  and  $^{137}\text{Cs}$  dating which imply a relative uniform accumulation at this site and a relatively uniform volumetric sedimentation rate of around  $0.19 \text{ cm y}^{-1}$ , with a slightly lower value since the 1950s (personal communication P. Appleby; visible in a slight flattening of the age-depth model in Fig. 4). According to the age-depth model based on the  $^{210}\text{Pb}$  and  $^{137}\text{Cs}$  dating, the short core, with a total length of 39 cm, spans a period of 222 years (ca. 2015–1793CE, mean ages). Hence, the mean sampling resolution of the record is sub-decadal with  $5.7 \pm 1.7$  years (min: 2, max: 10 years).

315

The four  $^{14}\text{C}$  ages of the bulk sediment show a clear offset to the  $^{210}\text{Pb}$  and  $^{137}\text{Cs}$  chronology, with significant older ages that nearly progressively get younger with depth (see Table 2). Comparing two dating results of the same sample depth (25–26 cm), we receive an  $^{14}\text{C}$  age of  $1806 \pm 20$   $^{14}\text{C}$  years BP (before present) which corresponds to a calibrated  $^{14}\text{C}$  age of 244 calibrated CE ( $2\sigma$  range: 210–256). The same sample was dated by the  $^{210}\text{Pb}$  and  $^{137}\text{Cs}$  method and received an age of  $1858\text{CE} \pm 11$ , resulting in an offset of 1614 years. A comparable high age difference in the surface sample was observed in another study at Lake Khamra (Glückler et al., 2021), using macrofossil as well as bulk sediment samples to retrieve  $^{14}\text{C}$  ages. Possible reasons were discussed such as an influence of dissolved carbonates, the so called hard-water effect (Björck and Wohlfarth, 2001; Philippsen, 2013), input of old organic carbon (Colman et al., 1996; Vyse et al., 2020) or mixing processes within the sediment (Biskaborn et al., 2012) which could have led to discontinuous  $^{14}\text{C}$  age development with depth. However, since the  $^{210}\text{Pb}$  and  $^{137}\text{Cs}$  dating results are very uniform to a depth of 26 cm and no interruption could be detected in the record, a mixing process is rather unlikely. At Lake Khamra, very old macrofossils can be transported into the lake and possibly influence the radiocarbon age within the bulk sediment (Glückler et al., 2021). The origin of old carbon from eroding permafrost cannot be ruled out either, as the area lies in a sporadic permafrost zone (Brown et al., 1997; Fedorov et al., 2018). Additionally, inorganic carbon can be transported into the lake by the main inflow as the catchment contains early Palaeozoic carbonates (Chelnokova et al., 1988; Glückler et al., 2021). Large age uncertainties make it very difficult to use  $^{14}\text{C}$  ages for records covering the last few hundred years (Björck and Wohlfarth, 2001). Since the old and non-continuous  $^{14}\text{C}$  ages are not consistent with the homogeneous and high-resolution  $^{210}\text{Pb}$  and  $^{137}\text{Cs}$  dating results, the  $^{14}\text{C}$  dating results are excluded from the age-depth model.

335

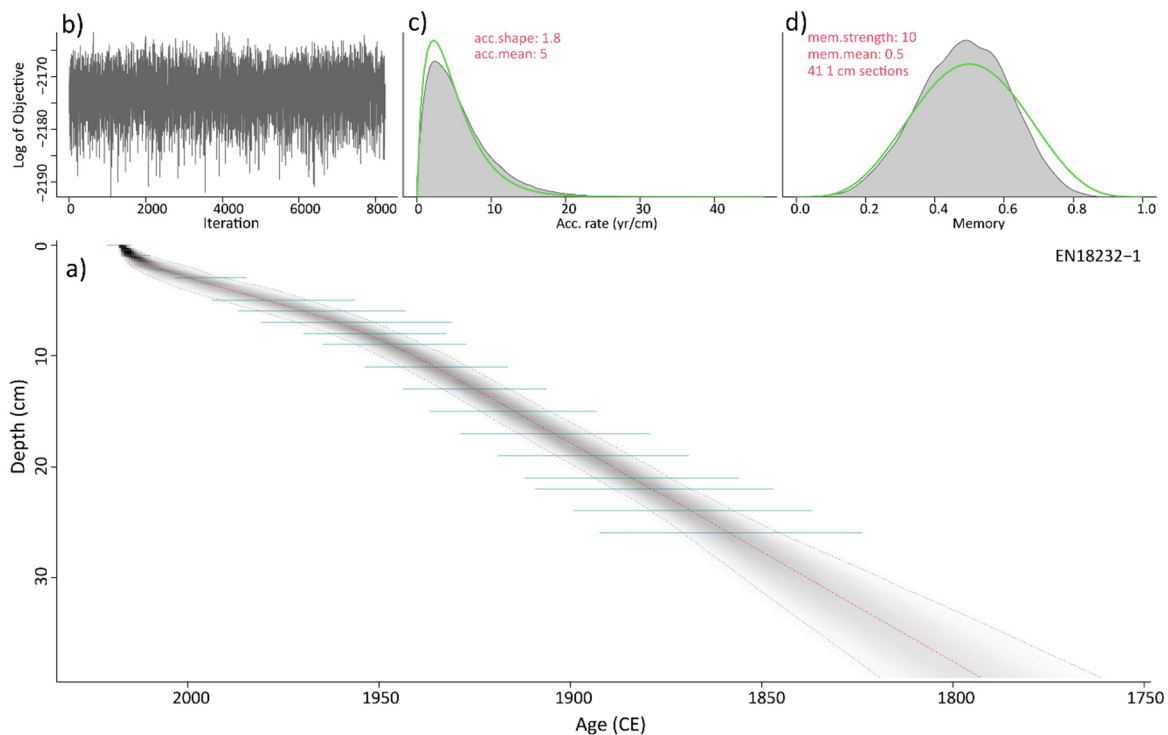


**Figure 4.** a) Bayesian accumulation model applying R package ‘rbacon’ (Blaauw and Christen, 2011) based on the  $^{210}\text{Pb}$  and  $^{137}\text{Cs}$  dating (green lines) of the short core EN18232-1 (grey lines= $2\sigma$  range; red line=median). b) Model iteration log. c, d) Prior (green line) and posterior (grey area) distributions for accumulation rate and memory, respectively.

340

**Table 2. Results <sup>14</sup>C ages of the bulk sediment samples EN18232-1.**

Lab-ID	Depth (cm)	F <sup>14</sup> C	+-(abs)	<sup>14</sup> C Age BP	+-(y)	Cal Age median [CE]	Cal Age min [CE] (2 sigma)	Cal Age max [CE] (2 sigma)	Cal Age median [BP]	Cal Age min [BP] (2 sigma)	Cal Age max [BP] (2 sigma)
EN18232-1_26	25-26	0.7987	0.0020	1,806	20	244	210	256	1706	1694	1740
EN18232-1_31	30-31	0.8415	0.0016	1,387	15	651	640	664	1299	1286	1310
EN18232-1_35	34-35	0.8708	0.0016	1,111	15	944	939	991	1006	959	1011
EN18232-1_38	37-38	0.8623	0.0016	1,190	15	842	818	888	1108	1062	1132

### 4.3 $\delta^{18}\text{O}_{\text{diatom}}$ record

345 The diatom  $\delta^{18}\text{O}$  record of Lake Khamra (EN18232-1) covers approximately the last 220 years (ca. 2015–1790CE, mean ages; n=39). The overall mean  $\delta^{18}\text{O}_{\text{diatom}}$  is +21.7‰ varying by  $\pm 2.8\%$ , with a standard deviation of  $\pm 0.6\%$ . The absolute minimum is +20.6‰ at about 1940CE, 1915CE and 1875CE. The absolute maximum of +23.4‰ occurs at circa 1955CE. Contamination correction increased all measured  $\delta^{18}\text{O}$  values by a mean of +0.3‰ with a narrow range of between +0.2‰ and +0.4‰ (Fig. 5). This indicates a very low degree of contamination after

350 cleaning, and an overall low correction within or close to the analytical error of  $\pm 0.25\%$ . The trend before and after contamination correction remains identical (-0.0006; n=39) which implies uniformly prepared sample material, where the correction has no (significant) effect on the course of the record. All descriptions refer to the corrected values (referred to as  $\delta^{18}\text{O}_{\text{diatom}}$ ).

#### 355 4.3.1 Phases of the Lake Khamra $\delta^{18}\text{O}_{\text{diatom}}$ record

We identify four phases (I–IV) into which the  $\delta^{18}\text{O}_{\text{diatom}}$  time series of Lake Khamra is subdivided (Fig. 5). This differentiation from top to bottom of the core is mainly based on the deviation from the overall mean  $\delta^{18}\text{O}_{\text{diatom}}$  value of +21.7‰. The description of phases begins with the most recent segment of the core and progresses towards the older sections, as the following discussion first validates the youngest part of the record with

360 meteorological data.

##### Phase I (2015–1970CE, n=5)

In the most recent phase I,  $\delta^{18}\text{O}_{\text{diatom}}$  of Lake Khamra shows values mostly below the overall mean with a low variability of  $\pm 1.2\%$ , a mean of +21.5‰ and a standard deviation of  $\pm 0.4\%$ . Main characteristics are a continuous

365 decrease since ca. 1970CE with a clear minimum at ca. 2000CE (Fig. 5). Since 2000CE,  $\delta^{18}\text{O}_{\text{diatom}}$  increases slightly, but still remains below the absolute mean value.

##### Phase II (1970–1930CE, n=6)

In contrast to phase I,  $\delta^{18}\text{O}_{\text{diatom}}$  values in phase II are enriched in heavy isotopes above the overall mean including

370 the absolute maximum (+23.4‰) at around 1950CE, with only one depleted value, a minimum, at about 1940CE

(+20.6‰). This results in the largest variability of  $\pm 2.8\text{‰}$  of the entire  $\delta^{18}\text{O}_{\text{diatom}}$  record, a clearly elevated mean value of +22.3‰ and a standard deviation of  $\pm 1\text{‰}$ . The maximum reaches a z-score of +2.7, the minimum has a negative score of -1.8.

375 Phase III (1930–1830CE, n=20)

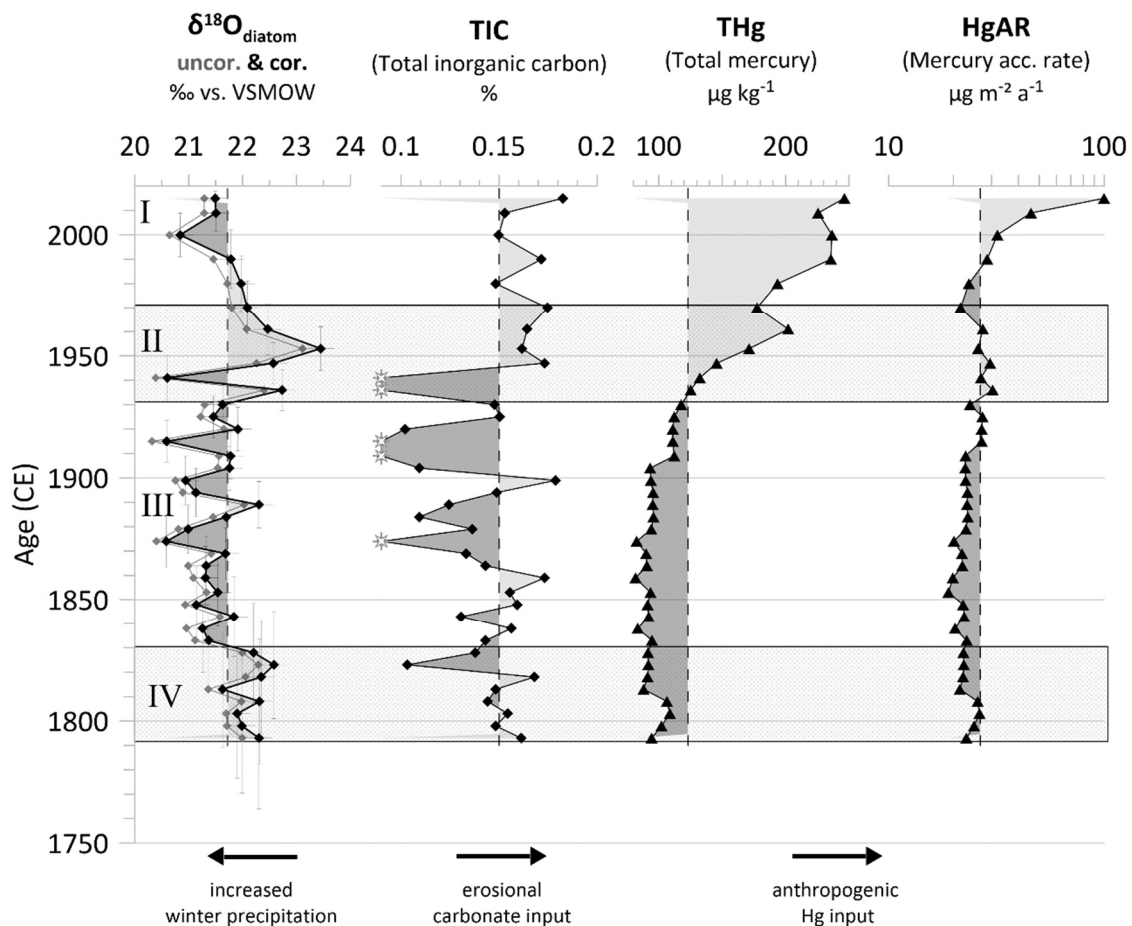
Phase III consists of depleted  $\delta^{18}\text{O}_{\text{diatom}}$  values, mainly below the overall mean, which begins rather abruptly around 1830CE and persists until around 1930CE whereby it varies by  $\pm 1.7\text{‰}$ . It is the longest phase of the diatom record (ca. 100 years), with the lowest mean value of all phases (+21.4‰), also including two absolute minima (+20.6‰ at ca. 1915CE and 1875CE), each with a z-score of -1.8. The standard deviation is comparable to phase I ( $\pm 0.4\text{‰}$ ).

380

Phase IV (1830–1790CE, n=8)

Phase IV of the Khamra record is characterised by notably enriched  $\delta^{18}\text{O}_{\text{diatom}}$  values, primarily above the absolute mean. The internal mean of +22.2‰ is similar to phase II but less pronounced with a variability of  $\pm 1\text{‰}$  and a standard deviation of only  $\pm 0.3\text{‰}$  (Fig. 5).

385



390 **Figure 5.** Lake internal proxy records of the short core EN18232-1, Lake Khamra. I–IV indicate the four phases according to the  $\delta^{18}\text{O}_{\text{diatom}}$  record. Diatom  $\delta^{18}\text{O}$ : measured  $\delta^{18}\text{O}_{\text{diatom}}$  (grey line) and contamination-corrected  $\delta^{18}\text{O}_{\text{diatom}}$  values (black line) shown with analytical and chronological errors. Geochemical records: total inorganic carbon (TIC), white stars indicate values below detection limit. Mercury measurements are given in total mercury (THg, in  $\mu\text{g kg}^{-1}$ ) and converted into accumulation rates (HgAR, in  $\mu\text{g m}^{-2} \text{a}^{-1}$ ). The individual mean values are displayed as vertical dashed lines. Arrows indicate a possible interpretation of the proxy.

#### 4.4 Carbon and mercury concentrations (TIC, THg, HgAR)

395 From the onset of the record at about 1790CE to the 1950s, TIC measurements remain constant at or slightly below the overall mean of 0.15% (Fig. 5). At ca. 1875CE, 1910CE and 1940CE five samples are below the detection limit of <0.1%. At about 1950CE, TIC switch to above mean values, reaching a maximum of 0.18% in the uppermost sample.

400 THg shows a drastic increase and a tripling of the mercury concentrations in recent times (Fig. 5). All values are above the detection limit of 0.003ng. At the beginning of the record until around 1920CE, THg values fluctuate slightly between the minimum of 82  $\mu\text{g kg}^{-1}$  to 111  $\mu\text{g kg}^{-1}$ , below the mean of 123  $\mu\text{g kg}^{-1}$ . Since ca. 1930CE, THg rises nearly continuously, reaching the maximum of 246  $\mu\text{g kg}^{-1}$  in the topmost sample. The mercury accumulation rates have a mean of 26.6  $\mu\text{g m}^{-2} \text{a}^{-1}$  (18.9–99.8  $\mu\text{g m}^{-2} \text{a}^{-1}$ ). In the lower part of the short core, HgAR remains below or at the mean values (Fig. 5). Between about 1930CE to 1950CE, HgAR increases slightly above  
405 the mean before falling below the mean around the 1970s. Since then, we observe a drastic increase to the maximum value of 99.8  $\mu\text{g m}^{-2} \text{a}^{-1}$  in the youngest sample.



## 5 Discussion

### 5.1 Modern lake hydrology and isotopic signature of precipitation

410 The interpretation of the oxygen isotope record of lacustrine diatom silica ( $\delta^{18}\text{O}_{\text{diatom}}$ ) requires a careful consideration of the current hydrological conditions of the respective study site (Leng and Barker, 2006).  $\delta^{18}\text{O}_{\text{diatom}}$  is influenced directly and indirectly by various depleting and enriching factors, summarised in Meister et al. (2023). Beside the lake water temperature ( $T_{\text{lake}}$ ), the oxygen isotope composition ( $\delta^{18}\text{O}_{\text{lake}}$ ) and its sensitivity to evaporation also affects the  $\delta^{18}\text{O}_{\text{diatom}}$  signal. The water residence time of Lake Khamra has been modelled to about  
415 one year and three months (474 days; Messenger et al., 2016), which implies a nearly annual exchange of the lake water and hence the possibility of only seasonal evaporative effects. The water-depth profile, taken below the spring ice cover, confirms a well-mixed water column with only slight variations in  $\delta^{18}\text{O}_{\text{lake}}$  ( $\pm 0.3\text{‰}$ ) and no thermocline at least in March 2020 (Fig. 3b, c). Lake Khamra is an open lake system, with an outflow in the north-east (see Map Fig. 1b). In open lake systems,  $\delta^{18}\text{O}_{\text{lake}}$  generally mirrors the oxygen isotope signal of precipitation  
420 ( $\delta^{18}\text{O}_{\text{prec}}$ ), including the local precipitation intermittency (Leng and Barker, 2006). We compare  $\delta^{18}\text{O}_{\text{lake}}$  to  $\delta^{18}\text{O}_{\text{prec}}$  data of the nearest GNIP stations in Yakutsk and Irkutsk (Fig. 1a). The recent mean  $\delta^{18}\text{O}_{\text{lake}}$  at Khamra lake of  $-20.0\text{‰}$  (March 2020) is closest to the long-term annual weighted mean  $\delta^{18}\text{O}_{\text{prec}}$  of Yakutsk (Fig. 3a), but overall more depleted compared to Yakutsk, Irkutsk and the modelled annual mean  $\delta^{18}\text{O}_{\text{prec}}$  (Fig. 3a). Consequently, the offset of  $\delta^{18}\text{O}_{\text{lake}}$  towards depleted isotope composition indicates that the water of Lake Khamra is strongly  
425 influenced by isotopic light precipitation, likely snow or snowmelt originating during the cold winter months (Fig. 2). The similarity of the  $\delta^{18}\text{O}_{\text{lake}}$  to Yakutsk (Fig. 3a) might be explained by the overall lowest monthly mean values of  $\delta^{18}\text{O}_{\text{prec}}$  measured in Yakutsk, compared to Irkutsk and the regional modelled data (Fig. 2).  $\delta^{18}\text{O}_{\text{prec}}$  is temperature-dependent and increases in the global mean at rising air temperatures ( $T_{\text{air}}$ ) by  $+0.7\text{‰}/^{\circ}\text{C}$  (Dansgaard, 1964). Ascribed to the more northerly position of Yakutsk (Fig. 1a), it reveals the coldest annual mean  
430 temperatures compared to Vitim and Irkutsk ( $-9.3^{\circ}\text{C}$ , 1929–2018CE, Yakutsk, ECA station code: 3214) and thus most depleted  $\delta^{18}\text{O}_{\text{prec}}$  (Dansgaard, 1964).

The Khamra  $\delta^{18}\text{O}_{\text{lake}}$  measurements plot below the GMWL (Fig. 3a) and the water samples measured in March 2020 plot even slightly below the modelled LMWL (Fig. 3a), indicating potential evaporation effects at this site. The water samples taken in August and in March linearly correlate with a slope of 4.9 and an intercept of  $-60.6\text{‰}$   
435 ( $n=7$ ,  $R^2=0.99$ ), interpreted as evaporation line (EL; Fig. 3a), comparable with local ELs of Central Yakutian lakes (slope = 4.99;  $n=39$ ,  $R^2=0.95$ ; Wetterich et al., 2008). The intersection point of the EL with the modelled LMWL ( $\delta^{18}\text{O}$ :  $-20.9\text{‰}$ ,  $\delta\text{D}$ : of  $-164.0\text{‰}$ ) is assumed to reflect the  $\delta^{18}\text{O}$  of the mean influx to the lake and is nearly identical with the  $\delta^{18}\text{O}_{\text{lake}}$  measurement of August 2018 ( $\delta^{18}\text{O}_{\text{lake}}$ :  $-21.2\text{‰}$ ,  $\delta\text{D}_{\text{lake}}$ :  $-165.3\text{‰}$ ). This suggests that the August- $\delta^{18}\text{O}_{\text{lake}}$ -sample has a clear precipitation signal and evaporation effects are negligible, supported by its very low  
440 conductivity of  $40 \mu\text{S cm}^{-1}$  (Table 1). However, the  $\delta^{18}\text{O}_{\text{lake}}$  value measured in August 2018 is strongly depleted (Fig. 3a) and corresponds to a modelled monthly mean value of precipitation between November and December (Fig. 2). Since there is only one water sample measured in summer 2018 and the difference of  $1.2\text{‰}$  to the water samples in March 2020 is low, this single datapoint should be interpreted with caution. However, in summer an isotopically heavier  $\delta^{18}\text{O}_{\text{lake}}$  value would be expected due to higher summer temperatures, potential evaporation  
445 effects and the clear seasonality with enriched  $\delta^{18}\text{O}_{\text{prec}}$  in the summer months (Fig. 2). Hence, the inflow of melt water from either snow and/or glaciers in the catchment, which is isotopically light water, could lower  $\delta^{18}\text{O}_{\text{lake}}$ , as seen in other studies in Eurasia (Mackay et al., 2013; Meyer et al., 2015; Kostrova et al., 2021; Meyer et al., 2022).

Lake Khamra lies at a relatively low altitude of 340 m a.s.l, without glaciers in the catchment that could be responsible for the depleted meltwater input. We know from an expedition report (Biskaborn et al., 2021a), that a lot of snow can accumulate in this area, as observed in March 2020, revealing the lowest isotope composition of all analysed samples (Table 1). Therefore, enhanced snow meltwater input could lead to an isotopic depletion of the lake water, which can apparently last until the summer months.

## 5.2 Drivers of $\delta^{18}\text{O}_{\text{diatom}}$

Different factors determine the isotopic signature of diatom shells (Leng and Barker, 2006; Meister et al., 2023), which is directly controlled by  $T_{\text{lake}}$  and  $\delta^{18}\text{O}_{\text{lake}}$  during biosynthesis (Moschen et al., 2005; Dodd and Sharp, 2010). Leclerc and Labeyrie (1987) developed an equation based on the temperature-dependent fractionation between water and biogenic silica that can be used to reconstruct the water temperature conditions that prevailed during diatom shell formation. Applying the following Eq. (5), we use the recent measured  $\delta^{18}\text{O}_{\text{diatom}} = +21.5\text{‰}$  and the mean  $\delta^{18}\text{O}_{\text{lake}} = -20.0\text{‰}$ , measured in March 2020, to calculate a water-silica isotope fractionation factor of  $\alpha_{(\text{SiO}_2\text{-H}_2\text{O})} = 1.0423$ .

$$\alpha_{(\text{SiO}_2\text{-H}_2\text{O})} = (1000 + \delta^{18}\text{O}_{\text{diatom}})/(1000 + \delta^{18}\text{O}_{\text{lake}}) , \quad (5)$$

(Leclerc and Labeyrie, 1987)

Following the established isotope fractionation correlation, Eq. (6), between fossil diatom silica and water:

$$1000 \ln \alpha_{(\text{SiO}_2\text{-H}_2\text{O})} = 3.26 * 10^6 / T^2 + 0.45 , \quad (6)$$

(Leclerc and Labeyrie, 1987)

we derive a  $T_{\text{lake}}$  of  $+8.7^\circ\text{C}$  which is substantially higher than the mean  $T_{\text{lake}} = +2.5^\circ\text{C}$  measured in March 2020 below the ice. Calculating  $T_{\text{lake}}$  from  $\delta^{18}\text{O}_{\text{lake}}$  of  $-21.16\text{‰}$  as measured in August 2018 ( $\alpha_{(\text{SiO}_2\text{-H}_2\text{O})} = 1.0436$ ), we derive a temperature of  $+4.8^\circ\text{C}$ . The calculated water temperature range ( $+4.8$  to  $+8.7^\circ\text{C}$ ) seems realistic in the early summer months when the ice cover of Lake Khamra starts to melt (May is the first month in which monthly mean  $T_{\text{air}} > 0^\circ\text{C}$ , 1928–2019CE, Vitim, Fig. 2). Further analyses on the short core EN18232-1 comprise diatom assemblages, which will be the focus of a follow-up study and are therefore not included here. Overall, the planktonic diatom genera *Aulacoseira* (Thwaites) is by far the most abundant and consists mainly of the planktonic species *Aulacoseira subarctica* (O. Müller), which growth conditions (Gibson et al., 2003) agree very well with the reconstructed water temperature range. It is assumed that in lake systems the effect of diatom species-dependent isotope fractionation, the so called vital-effect, is negligible (Shemesh and Peteet, 1998; Rosqvist et al., 1999; Shemesh et al., 2001; Leng and Barker, 2006; Chaplignin et al., 2012b). Since the genus *Aulacoseira* builds up heavy and highly silicified diatom frustules (Laing and Smol, 2003), it likely also dominates the diatom biomass, and hence the isotopic signal. Using Eq. (6) with  $\delta^{18}\text{O}_{\text{lake}}$  and  $T_{\text{lake}}$  measured in March 2020, we can calculate an expected, recent  $\delta^{18}\text{O}_{\text{diatom}}$  of  $+23.4\text{‰}$ . The calculated  $\delta^{18}\text{O}_{\text{diatom}}$  is enriched by  $+1.9\text{‰}$  compared to the actual measured surface  $\delta^{18}\text{O}_{\text{diatom}}$  value ( $+21.5\text{‰}$ ), likely due to the very low water temperature measured in March, which probably does not correspond to the diatom growth temperature as discussed above. Nevertheless, as the

reconstructed water temperatures aligns with the dominant diatom species, the  $\delta^{18}\text{O}_{\text{diatom}}$  record of Lake Khamra is generally assumed to be suitable for palaeoclimate reconstructions.

490 Globally,  $T_{\text{air}}$  and  $\delta^{18}\text{O}_{\text{prec}}$  have a positive fractionation coefficient of  $+0.7\text{‰}/\text{°C}$  (Dansgaard, 1964), which compensates the fractionation of biosynthesis between  $T_{\text{lake}}$  and  $\delta^{18}\text{O}_{\text{lake}}$  ( $-0.2\text{‰}/\text{°C}$ , Moschen et al., 2005; Dodd and Sharp, 2010). As a consequence,  $T_{\text{air}}$  has a stronger effect on  $\delta^{18}\text{O}_{\text{prec}}$ , linked with  $\delta^{18}\text{O}_{\text{lake}}$  at Lake Khamra, than  $T_{\text{lake}}$  and therefore on  $\delta^{18}\text{O}_{\text{diatom}}$ . This tendency is visible in other  $\delta^{18}\text{O}_{\text{diatom}}$  studies of the Northern Hemisphere (Meyer et al., 2015; Chaplignin et al., 2016; Broadman et al., 2022). The fractionation coefficient is significantly  
495 higher ( $+0.81\text{‰}/\text{°C}$ ) than the global coefficient, when using the monthly average  $T_{\text{air}}$  values of the weather station in Vitim and the monthly modelled  $\delta^{18}\text{O}_{\text{prec}}$  values ( $n=12$ ) for the region (Bowen et al., 2005; Bowen, 2023; IAEA/WMO, 2023). The distinct seasonality of  $\delta^{18}\text{O}_{\text{prec}}$  highlights its strong  $T_{\text{air}}$  dependency at the Lake Khamra region, following the high annual  $T_{\text{air}}$  range of  $47\text{°C}$  (Fig. 2). Therefore, we conclude the  $T_{\text{air}}$  dependent fractionation of precipitation overprints the fractionation due to biosynthesis and hence  $T_{\text{air}}$  has a stronger effect  
500 on the  $\delta^{18}\text{O}_{\text{diatom}}$  record and its variations shape palaeoclimate trends rather than  $T_{\text{lake}}$ .

### 5.3 Comparison of $\delta^{18}\text{O}_{\text{diatom}}$ with meteorological data since 1930CE including lake internal proxies

The comparison of the diatom isotope record with meteorological data of Vitim, starting in the 1930s (Fig. 6), enables the validation of the variability of the  $\delta^{18}\text{O}_{\text{diatom}}$  record, including factors as  $T_{\text{air}}$ , evaporation, precipitation  
505 and seasonality, at least in the upper part of the record (phases I and II).

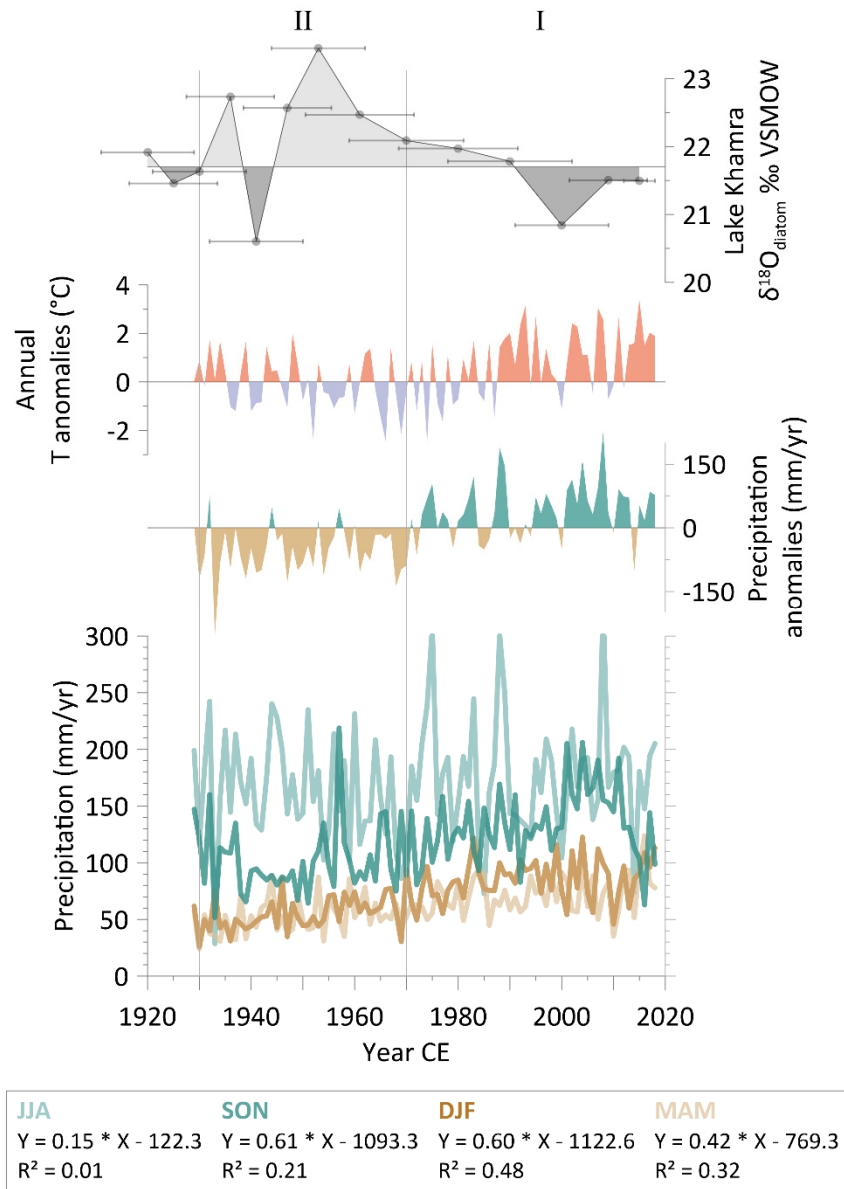
In phase I, we see an overall depletion of  $\delta^{18}\text{O}_{\text{diatom}}$  values. Contrary, annual  $T_{\text{air}}$  rises and shows almost continuous positive anomalies since about the 1980s reaching up to  $+3.4\text{°C}$  (Fig. 6). Rising  $T_{\text{air}}$  would lead to enriched  $\delta^{18}\text{O}_{\text{prec}}$  values (Dansgaard, 1964), followed by rising  $\delta^{18}\text{O}_{\text{lake}}$  and  $\delta^{18}\text{O}_{\text{diatom}}$  values. Moreover, an increase in  $T_{\text{air}}$  probably leads to stronger evaporative effects which would even further enrich  $\delta^{18}\text{O}_{\text{lake}}$  and hence  $\delta^{18}\text{O}_{\text{diatom}}$ , as observed  
510 within the recent sediment samples of a  $\delta^{18}\text{O}_{\text{diatom}}$  record in Alaska (Broadman et al., 2020). If we assume  $T_{\text{air}}$  as major control, we would expect a continuous increase in  $\delta^{18}\text{O}_{\text{diatom}}$ . As a consequence,  $T_{\text{air}}$  cannot explain the observed, recent depletion in  $\delta^{18}\text{O}_{\text{diatom}}$  and likely plays a subordinate role, at least in phase I.

However, we see a significant increase in total rainfall amounts in the study area, illustrated by almost consistently positive annual precipitation anomalies during phase I (Fig. 6). An increase in precipitation in addition to rising  
515 temperatures would buffer evaporation effects and thus potentially weaken the increase of  $\delta^{18}\text{O}_{\text{lake}}$  due to rising  $T_{\text{air}}$ . This is supported by the isotope composition of the recent lake water samples, which show only a minor effect of evaporation (Fig. 3a). In order to achieve a decrease in  $\delta^{18}\text{O}_{\text{diatom}}$  resulting from higher precipitation levels, a greater quantity of isotopically depleted water has to reach the lake to be incorporated into the diatom frustules. Most depleted  $\delta^{18}\text{O}_{\text{prec}}$  falls during cold seasons, mainly as snow, when regional monthly mean temperatures are  
520 below  $0\text{°C}$  for seven months (October to April, Fig. 2). All three cold seasons (September-October-November: SON; December-January-February: DJF; March-April-May: MAM) show a more pronounced precipitation increase compared to only a slight increase during the summer months (June-July-August: JJA, Fig. 6). The highest increase is recorded during SON seasons ( $+0.61\text{ mm yr}^{-1}$ ,  $R^2=0.2$ ) and DJF ( $+0.60\text{ mm yr}^{-1}$ ,  $R^2=0.5$ ). Consequently, the overall increase in annual precipitation is likely mainly due to the increase in winter precipitation. Several  
525 studies discuss a change of snowfall amount over Eurasia in recent decades probably as a result of extreme temperature rises in the Arctic, leading to loss of sea ice and increased evaporation over the Arctic Ocean (Ghatak et al., 2010, 2012; Wegmann et al., 2015; Bailey et al., 2021; Sato et al., 2022). Increased moisture amounts are

transported southwards leading to increased snowfall and duration of snow cover between 1966–2007CE in specific areas in Eurasia, including Yakutia (Bulygina et al., 2009). During SON, the second largest amount of annual precipitation is received (Fig. 2), and may contribute significantly to  $\delta^{18}\text{O}_{\text{lake}}$ . Most precipitation during SON season is expected to fall as snow (monthly mean  $T_{\text{air}}$  Vitim: September: 6.4°C; October: -3.3°C; November: -18.0°C; 1929–2018CE) with highly depleted  $\delta^{18}\text{O}$  values (Fig 3a). The snow can accumulate in the catchment and lead to a depletion of  $\delta^{18}\text{O}_{\text{lake}}$  and, thus, of  $\delta^{18}\text{O}_{\text{diatom}}$  when it reaches the lake as meltwater in the next spring season. The influence of snowmelt and its varying amount as controlling factor on the diatom isotopes has been observed in other lacustrine  $\delta^{18}\text{O}_{\text{diatom}}$  records in northern latitudes (Mackay et al., 2013; Rosqvist et al., 2013; Broadman et al., 2022; Meyer et al., 2022).

Increased snowmelt runoff might increase (soil) erosion within Lake Khamra's catchment. Occurrence of dolomite and limestone in the bedrock (Chelnokova et al., 1988) are a possible source for total inorganic carbon (TIC) in the sediment (Fig. 5), probably contributing to the observed  $^{14}\text{C}$  age offset (see 4.2). At the Russian lake Bolshoye Shchuchye, elevated TIC values are used as a proxy for erosion and sediment supply from detrital carbonate in the bedrock (Lenz et al., 2021). Overall, measured TIC values at Lake Khamra are low. The consistently above-average TIC values in phase I are comparable to a deglaciation period described at Lake Bolshoye Shchuchye, supporting our argument of possible erosional input from the catchment (Fig. 5). Nevertheless, there are possible other sources for TIC in lake sediments, like biogenic carbonate sources, including carbonate fossils. As they are absent in the Khamra sediments, it is a rather unlikely TIC source. Since the pH value of 6 of the modern Lake Khamra indicates acidic conditions with rather cold lake water temperature, an autochthonous calcite precipitation as source of TIC (Cohen et al., 2003) seems rather unlikely, too. However, to exclude the presence of carbonate minerals with certainty, an SEM analysis of the sediment would be required (Last and Smol, 2001), which is beyond the scope of this study.

Mercury levels (THg) exhibit a continuous increase and significant enrichment (Fig. 5), clearly surpassing the naturally occurring mercury concentrations measured in Yakutian permafrost, with a background signal of  $5.21 \pm 3.66 \mu\text{g kg}^{-1}$  (Rutkowski et al., 2021). Mercury is known to be deposited in lake sediments due to human pollution by different anthropogenic sources such as air fallout, erosion, mining, agriculture as well as industry and urban waste waters (Wang et al., 2004). Lake Khamra is very pristine, with no great industry or urban settlements in the close vicinity. It is likely that mercury reaches Lake Khamra by air pollution, comparable to Lake Bolshoe Toko, another pristine Russian lake (Biskaborn et al., 2021b). The mercury accumulation rates (HgAR) show a more than fourfold increase in phase I, corresponding to mercury fluxes observed at Lake Baikal post 1850CE, especially in the south basin and the Selenga Delta (Roberts et al., 2020). We assume that the rising HgAR at Lake Khamra, especially since the 1990s (Figure 5), may be connected with the concurrent industrialisation in Asia, dominated by China and India, and the associated Hg emissions (Pacyna et al., 2016; Sundseth et al., 2017), as discussed in Roberts et al. (2020).



565 **Figure 6.** Khamra  $\delta^{18}\text{O}_{\text{diatom}}$  record with age uncertainties of the corresponding phase I and II, compared to annual temperature anomalies and annual precipitation anomalies of Vitim, 1929–2018CE, 90 yrs., reference period 1961–1990CE. Below: Seasonal variation of precipitation amount 1929–2018CE, 90 yrs., displayed in different seasons: June, July, August (JJA), September, October, November (SON), December, January, February (DJF), March, April, May (MAM), individual trends are shown in the box. All meteorological data of weather station Vitim (59.45° N, 112.58° E, 186 m a.s.l., ECA station code: 3235), data accessible via <https://climexp.knmi.nl> (Klein Tank et al., 2002).

570

Phase II is meteorologically characterised by a clear precipitation deficit, while temperatures indicate a rather moderate to cool period, contrary to phase I (Fig. 6). Rather cool temperatures cannot explain the enriched  $\delta^{18}\text{O}_{\text{diatom}}$  data due to the positive correlation between  $T_{\text{air}}$  and  $\delta^{18}\text{O}_{\text{diatom}}$ , whereas the precipitation deficit may provide an explanation. From about 1935CE to 1955CE, we see a clear reduction of SON precipitation (Fig. 6).

575

Less snow accumulation leads to less meltwater input in the following spring and hence possibly to less depleted  $\delta^{18}\text{O}_{\text{diatom}}$  values. The relative influence of summer precipitation (JJA) on  $\delta^{18}\text{O}_{\text{lake}}$  could increase and, with its enriched  $\delta^{18}\text{O}_{\text{prec}}$  values, could also lead to increased  $\delta^{18}\text{O}_{\text{diatom}}$  values. Additionally, evaporative effects due to the overall precipitation deficit in phase II might further increase  $\delta^{18}\text{O}_{\text{lake}}$  and, hence  $\delta^{18}\text{O}_{\text{diatom}}$ .

TIC shows a shift from below to above detection limit at around 1950CE, almost simultaneously with the change  
580 from a minimum to a maximum in  $\delta^{18}\text{O}_{\text{diatom}}$  (Fig. 5). However, an assumed enhanced erosional input from the  
catchment linked with elevated TIC, contrasts with the observed overall precipitation deficit in phase II. Mercury  
levels start to rise rapidly since 1930CE and show a first maximum around 1960CE, probably deposited by air  
pollution, as black carbon emissions quickly increased in Russia at that time (Eckhardt et al., 2023).

According to the correlation with regional meteorological data, air temperature alone cannot be the driving factor  
585 of  $\delta^{18}\text{O}_{\text{diatom}}$  at Lake Khamra. We assume that, at least in phase I and II, variability of precipitation is a key factor  
influencing the  $\delta^{18}\text{O}_{\text{diatom}}$  signal.

#### 5.4 Comparison of $\delta^{18}\text{O}_{\text{diatom}}$ and internal proxies beyond meteorological data

In contrast to phases I and II, there are no meteorological data covering phases III and IV. If we adopt the  
590 interpretation applied in phase I and II, the prolonged phase III, with the lowest  $\delta^{18}\text{O}_{\text{diatom}}$  mean value of all four  
phases, suggests a phase of dominant winter precipitation, comparable to phase I and overall rather constant  
hydroclimatic conditions at Lake Khamra (Fig. 5). Cool air temperatures along with generally more depleted  
 $\delta^{18}\text{O}_{\text{prec}}$  values likely lead to reduced  $\delta^{18}\text{O}_{\text{diatom}}$  values. Thus, together with possible increased winter precipitation,  
cold and wet periods have a reinforcing effect on  $\delta^{18}\text{O}_{\text{diatom}}$ , difficult to disentangle. Therefore,  $T_{\text{air}}$  as influencing  
595 factor cannot be ruled out in this part of the record and it is possible that the record changes from a precipitation-  
dominated to temperature-dominated regime, as seen in other studies (Meyer et al., 2015, 2022; Broadman et al.,  
2022). TIC values vary mainly below the mean, indicate rather negligible carbonate input from the catchment.  
Mercury levels stay nearly constant around  $100 \mu\text{g kg}^{-1}$ , also seen in phase IV (Fig. 5), which could be assumed  
as the baseline value of the short core in pre-industrial times. Mercury fluxes show also nearly constant values  
600 slightly below or along the mean ( $26.6 \mu\text{g m}^{-2} \text{a}^{-1}$ ). Slightly enriched HgAR values at about 1910CE are nearly  
identical with the fluxes observed at the south basin of Lake Baikal (1910CE:  $0.26 \text{ ng cm}^{-2} \text{ yr}^{-1}$ ; Roberts et al.,  
2020), even though there rather local industrialisation is given as cause.

In phase IV, following the interpretation and comparable to phase II, we would expect a rather dry period with  
reduced winter precipitation linked with distinct enriched  $\delta^{18}\text{O}_{\text{diatom}}$  values (Fig. 5). However, higher temperatures  
605 could also have led to enriched  $\delta^{18}\text{O}_{\text{diatom}}$  values, at the beginning of the record. Similar to phase III, a warm and  
simultaneously dry phase could have amplified the diatom isotope signal. As a consequence, in the older part of  
the record (phase III and IV) it stays yet indistinct, which factor is decisive for the  $\delta^{18}\text{O}_{\text{diatom}}$  variability and  $T_{\text{air}}$   
cannot be ruled out as the prevailing influence on the diatom isotopy.

#### 610 5.5 Comparison with regional to hemispherical proxy records

Prior to meteorological recordings, comparable high-resolution climate proxies of the region are rare. A charcoal  
record from a parallel sediment core of Lake Khamra (Glückler et al., 2021) is used as a regional wildfire proxy  
for the past 2200 years (Fig. 7, shown from 1750CE as “robust CHAR”, which accounts for accumulated  
uncertainties). Statistical analyses of this charcoal record reveal two maxima within the comparable time period  
615 interpreted as increased fire activity in the area: one around 1950CE, the other less pronounced in the early 1800s  
(Glückler et al., 2021). The increased fire activity corresponds very well with enriched  $\delta^{18}\text{O}_{\text{diatom}}$  values observed  
in phases II and IV (Fig. 7). As persistent dry conditions favour forest fires, the overlap supports the interpretation

of enriched  $\delta^{18}\text{O}_{\text{diatom}}$  corresponding to dry conditions with reduced winter precipitation at Lake Khamra. A reduction in snow accumulation might lead to less soil moisture availability after snowmelt and, coinciding with higher temperatures, an early end of snowmelt can force extreme wildfires in eastern Siberia (Scholten et al., 2022). In contrast, periods of low fire activity, indicated by a low level of “robust CHAR” (Glückler et al., 2021), coincide with the assumption of rather wet periods with increased winter precipitation seen in phase I and III of the  $\delta^{18}\text{O}_{\text{diatom}}$  record (Fig. 7). Snow accumulation might not only increase soil moisture, but a prolonged snow cover duration, observed since 1966CE in Yakutia (Bulygina et al., 2009), might also limit the duration of the subsequent annual fire season.

Other diatom isotope studies on the Northern Hemisphere indicate a correlation with solar insolation on millennial time scales (Swann et al., 2010; Kostrova et al., 2019, 2021; Meyer et al., 2022). Insolation mainly influences  $T_{\text{air}}$  and, thus,  $\delta^{18}\text{O}_{\text{prec}}$ . The maxima of  $\delta^{18}\text{O}_{\text{diatom}}$  and in fire activity around 1950CE coincide with the modern maximum of insolation (Coddington et al., 2015) and a temperature peak in the Northern Hemisphere (McKay and Kaufman, 2014), which reinforces the interpretation of a dry period in phase II, whereby increased  $T_{\text{air}}$  could even amplify the enriched  $\delta^{18}\text{O}_{\text{diatom}}$  values. In contrast, the enriched  $\delta^{18}\text{O}_{\text{diatom}}$  values in phase IV and the charcoal peak around 1800CE (Glückler et al., 2021) overlap with the coldest reconstructed temperatures of the comparable period (McKay and Kaufman, 2014) and with the Dalton Minimum, a period of low sunspot activity between circa 1790CE and 1830CE, which coincided with the eruption of Mount Tambora in Indonesia in 1815CE. This volcanic eruption is considered as one of the largest in recent centuries (Zielinski et al., 1994; Bradley, 2015) and resulted in a significant drop of global air temperatures and led, among others, to an increase of the polar sea ice extent (Stenchikov et al., 2009). In addition, there was significantly less precipitation for over a decade, including regions north of  $40^\circ\text{ N}$  (Kandlbauer et al., 2013), overlapping with a reported dry period from 1750CE to 1820CE based on a tree ring  $\delta^{18}\text{O}$  moisture reconstruction from Northeast China (Liu et al., 2022). As a consequence, the Dalton Minimum and the corresponding low temperatures must have had a subordinate effect on the  $\delta^{18}\text{O}_{\text{diatom}}$  record, as the oxygen isotopes of diatoms are, in general, positively correlated with temperature and a reduction in temperature would lead to a depletion in  $\delta^{18}\text{O}_{\text{diatom}}$ . Therefore, the increased  $\delta^{18}\text{O}_{\text{diatom}}$  values in phase IV also likely correspond to dry conditions, and temperature as well as insolation can largely be excluded as driving force. Furthermore, the occurrence of dry conditions around these times serves as a potential explanation for increased fire activity despite cool temperatures.

Cooler temperatures and an expanded sea ice coverage across the Arctic Ocean (Stenchikov et al., 2009) during phase IV might have resulted in a diminished inland moisture transport (especially during the winter months), potentially contributing to drier conditions in the Lake Khamra region. A 30-year smoothed and normalised winter North Atlantic Oscillation (NAO) reconstruction (Trouet et al., 2009) indicates high variability over the comparable time period (Fig. 7), whereby negative values signify a diminished pressure gradient and a weakening of the westerlies, resulting in a reduced eastward moisture transport potential (Hurrell, 1995; Osborn, 2006; Hurrell and Deser, 2010). This could favour dry conditions within the Khamra region, whereas a positive NAO phase can increase winter precipitation by enhanced westerlies and a promoted moisture transport. The significant negative NAO peak during phase II (reduced winter precipitation) and the transition to a positive state in phase I (possible snow-rich) corresponds to the regional meteorological data (Fig. 6) and is consistent with the hydroclimatic interpretation of the diatom record. The strong negative phase in the NAO reconstruction between 1750CE and 1800CE does not directly correspond to the increased diatom values in phase IV (Fig. 7). However, a previous significant negative NAO phase may have already favoured dry conditions in the region, promoted by the observed

increase in fire frequency already since 1750CE (Glückler et al., 2021) and a dry period recorded by the moisture reconstruction from Northeast China (Liu et al., 2022).

Although the temperature and insolation trends in phase II (rather warm, high insolation) and IV (rather cool, low insolation) are opposite, but in both phases the Khamra  $\delta^{18}\text{O}_{\text{diatom}}$  values are isotopically enriched, we conclude that temperature and insolation likely play a minor role as prevailing influence on our diatom record. The good agreement of the Khamra  $\delta^{18}\text{O}_{\text{diatom}}$  record with the local charcoal record and the winter NAO index contribute to identify past hydroclimate variability. This strengthens the argumentation that variations in precipitation dominate the  $\delta^{18}\text{O}_{\text{diatom}}$  signal, extending to the earlier phases prior to meteorological observations.

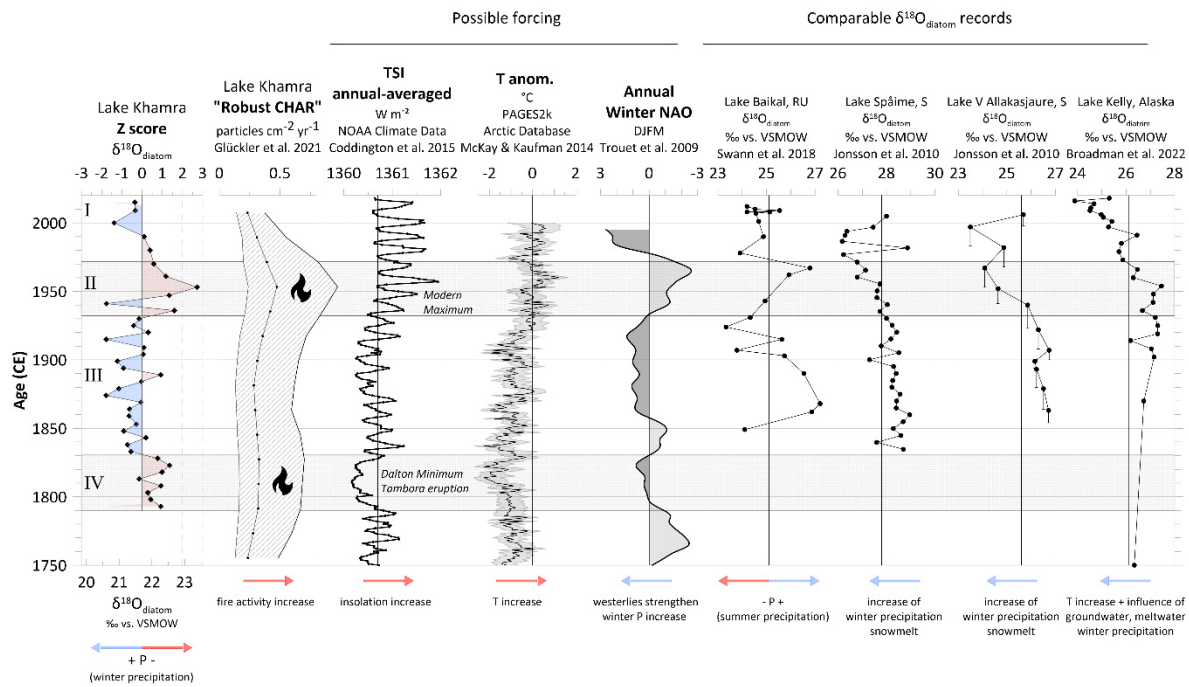


Figure 7. The Khamra diatom oxygen isotope record shown as absolute values and z-scores, in comparison to possible forcing and comparable diatom  $\delta^{18}\text{O}$  records. The proxies for comparison include a charcoal record of Lake Khamra (Glückler et al., 2021), annual averaged total solar insolation TSI (Coddington et al., 2015), a reconstructed temperature anomaly for the Arctic (McKay and Kaufman, 2014) and a multi-decadal winter North Atlantic Oscillation (NAO) reconstruction (Trouet et al., 2009). Comparable  $\delta^{18}\text{O}$  records include a record from Lake Baikal (Swann et al., 2018), two Swedish lakes (Jonsson et al., 2010), and a study from Alaska (Broadman et al., 2022). Arrows give individual interpretation. Vertical lines indicate the individual mean values.

### 5.6 Comparable high-resolution $\delta^{18}\text{O}_{\text{diatom}}$ records (regional and on the Northern Hemisphere)

There are very few high-resolution  $\delta^{18}\text{O}_{\text{diatom}}$  records in northern latitudes covering the same time period that can be considered for comparison. For Russia we only found one high-resolution, decadal-scale diatom isotope study of the southern basin of Lake Baikal (Fig. 1a; Swann et al., 2018). It includes a composite  $\delta^{18}\text{O}_{\text{diatom}}$  record for the period 2010–1850CE (160 yrs). The authors interpret their  $\delta^{18}\text{O}_{\text{diatom}}$  values contrary to the Khamra record. Low  $\delta^{18}\text{O}_{\text{diatom}}$  do not correspond to an increase, but to a decrease in precipitation, presumably because isotopically enriched summer precipitation dominates the Baikal record linked with the Atlantic Multi-decadal Oscillation (Sun et al., 2015; Swann et al., 2018), rather than heavily depleted winter precipitation at Lake Khamra, which is linked with the NAO. Furthermore, there are two high-resolution  $\delta^{18}\text{O}_{\text{diatom}}$  records from high-altitude sub-Arctic lakes in Scandinavia (Figs. 1a and 7), covering the period from about 2005–1835CE (Jonsson et al., 2010). Here, decreasing  $\delta^{18}\text{O}_{\text{diatom}}$  values are linked with increased winter precipitation, entering the lake as snowmelt,



coinciding with a high NAO index (Jonsson et al., 2010). This is a very similar interpretation to the Khamra record and supports it as proxy for winter precipitation and snowmelt. Similar context of snow-dominated lacustrine environments has been found for Kamchatka (Meyer et al., 2015) and the Polar Urals (Meyer et al., 2022), albeit  
690 on longer timescales. In Alaska, a multi-proxy palaeoclimate study includes a high-resolution  $\delta^{18}\text{O}_{\text{diatom}}$  record from Kelly Lake on the Kenai Peninsula (Fig. 1a), spanning the last 120 years (2018–1902CE; Broadman et al., 2022). The record is interpreted as a hydroclimate proxy, where the temperature effect is also superimposed by various hydroclimatic variables (Leng and Barker, 2006; Broadman et al., 2022), corresponding to the  $\delta^{18}\text{O}_{\text{diatom}}$  interpretation of Lake Khamra. There is another diatom isotope study on Kenai Peninsula (Broadman et al., 2020)  
695 focussing on millennial time scale hydroclimatic changes but including a high-resolution part (2018–1902 CE). Comparison with meteorological data reveals that  $\delta^{18}\text{O}_{\text{diatom}}$  in Alaska is mainly driven by the precipitation and evaporation balance (P-E).

All  $\delta^{18}\text{O}_{\text{diatom}}$  records of the mentioned studies (Jonsson et al., 2010; Swann et al., 2018; Broadman et al., 2020, 2022) are significantly enriched in heavy isotopes compared to the Khamra  $\delta^{18}\text{O}_{\text{diatom}}$  record (Fig. 7). The offset in  
700  $\delta^{18}\text{O}_{\text{diatom}}$  between these study sites is mainly due to considerably cooler  $T_{\text{air}}$ , and the distinctly continental climate of the Lake Khamra region and its reflection in  $\delta^{18}\text{O}_{\text{prec}}$ . All compared  $\delta^{18}\text{O}_{\text{diatom}}$  records shown in Fig. 7 indicate a decreasing trend and a striking shift towards enriched  $\delta^{18}\text{O}_{\text{diatom}}$  values in the youngest samples. Lake Khamra record has no overall decreasing trend since 1850CE, but after 1950CE the Khamra record shows a clear decreasing trend until 2000CE, with a rise in the youngest two samples (Fig. 7).

705 The Lake Baikal record (Swann et al., 2018) also has two minima at the onset of the 20<sup>th</sup> century and a maximum in the 1970s, comparable to the Lake Khamra record. The enriched  $\delta^{18}\text{O}_{\text{diatom}}$  values between 1850CE and 1950CE do not fit to the overall below  $\delta^{18}\text{O}_{\text{diatom}}$  mean values of the Khamra record in phase III. Extreme regional differences between these two lakes, such as catchment size and water residence time, as well as different development of summer and winter precipitation, probably lead to contrary interpretation.

710 Jonsson et al. (2010) reports a peak around 1980CE in both Swedish  $\delta^{18}\text{O}_{\text{diatom}}$  records (Fig. 7), delayed compared to the peak at the 1950s within the Khamra record, but also potentially attributed to a reduced ratio of winter-to-summer precipitation during that period. In general, the Swedish site shares similarities with the Khamra region in terms of NAO-driven winter precipitation fluctuations. Nevertheless, the  $\delta^{18}\text{O}_{\text{diatom}}$  increase after 1990CE is seen as a result of decreasing winter precipitation and simultaneous rising summer precipitation as well as rising  
715 annual temperatures (Jonsson et al., 2010), whereas winter precipitation and air temperature increased in the Lake Khamra region (Fig. 6). Remaining regional differences in hydroclimate, such as the influence of the Arctic Ocean on precipitation in the Khamra region, probably lead to the different extent of increase in the two records after 1990CE.

The  $\delta^{18}\text{O}_{\text{diatom}}$  record of Kelly lake is similar to the Khamra record in phase I and II, with a maximum in the 1950s  
720 and a decrease afterwards. The authors relate this decrease to an increasing amount of depleted winter precipitation due to a reduction of sea ice extent, depleted glacial meltwater originating from the glaciers, and/or depleted groundwater fed by glacial meltwater (Broadman et al., 2022). Unfortunately, there are no data available on groundwater conditions at Lake Khamra. Since there are no glaciers in the catchment of Lake Khamra, which could contribute to an isotopic decrease, the interpretation of Khamra  $\delta^{18}\text{O}_{\text{diatom}}$  as winter precipitation proxy is  
725 strengthened.

Consequently, the regional setting strongly influences the characteristics of each diatom record, requiring an individual consideration for data interpretation and cross-site comparisons. Nonetheless, this comparison reveals

similar hydroclimate reactions that support Lake Khamra's interpretation and strengthens the significance of the Khamra diatom record as a hydroclimate proxy, not only locally, but also cross-regionally with contrasting large-scale hydrological patterns.

### 5.7 Hydroclimatic anomalies covered by the Khamra $\delta^{18}\text{O}_{\text{diatom}}$ record

Our investigations reveal that the Khamra  $\delta^{18}\text{O}_{\text{diatom}}$  record can be interpreted as a hydroclimate proxy for winter precipitation variability whereby  $T_{\text{air}}$  has a rather subordinate effect on  $\delta^{18}\text{O}_{\text{diatom}}$ . Hence, extreme values in the  $\delta^{18}\text{O}_{\text{diatom}}$  record of Lake Khamra are most likely linked to dry/less snow (maxima) or wet/increased snow (minima) phases. Considering that Lake Khamra's residence time is modelled to about one year and three months (474 days; Messenger et al., 2016) and age uncertainties limit the resolution of our record, multi-day precipitation anomalies are unlikely to be captured by the diatom record. Consequently, a hydroclimatic anomaly must be of a "prolonged" or "persistent" nature (i.e. several dry or moist years in a row) or must lead to a lasting change in the conditions in the catchment area to have an impact detectable within our sub-decadal diatom record.

The minima of the continuous  $\delta^{18}\text{O}_{\text{diatom}}$  record occur in phase III and in phase II, whereas the maximum occurs in phase II. Thus, the short phase II (1970–1930CE,  $n=6$ ) is characterised by the highest variability within this record. Hence, this is interpreted as a period with an increased probability of hydroclimatic anomalies with rapidly changing and/or exceptional environmental conditions. The maximum in 1950CE lies outside the 99% percentile and z-score analysis confirms the exceptionally high value, as it is the only one deviating by nearly 3 times the standard deviation within the record (Fig. 7). This maximum can be ruled out as a measurement error or outlier as the sample has been measured in duplicate. Moreover, the values before and after it support this maximum. Elevated  $\delta^{18}\text{O}_{\text{diatom}}$  values correspond to elevated  $\delta^{18}\text{O}_{\text{lake}}$  values, likely caused by diminished meltwater input. Between 1935CE and 1955CE a decrease in autumn (SON) precipitation is evident which lies in an overall period of precipitation deficit in the region until the late 1960s (Fig. 6). The precipitation reduction corresponds to a prolonged negative phase of winter NAO (Fig. 7), with a minimum in the 1960s (Trouet et al., 2009). Moreover, the  $\delta^{18}\text{O}_{\text{diatom}}$  maximum at 1950CE coincides well with a clear maximum of regional wildfire activity (Glückler et al., 2021, Fig. 7). Vegetation surveys, carried out during the 2018 expedition (Kruse et al., 2019), revealed extensive regions of forest succession without less dense forest cover in the vicinity of Lake Khamra. Remote sensing data on historical forest fires and forest loss reach back to 2000CE only (Hansen et al., 2013; Giglio et al., 2018). We hypothesise that wildfires, which likely occurred in the 1950s and correspond to the observed dry period, had a considerable high impact destroying the dense forest in the lake's vicinity and resulting in the formation of large forest succession areas afterwards, which can be observed today. An increase of *Cyperaceae* pollen and more evergreen versus deciduous arboreal pollen types in the 1950s (Glückler et al., 2021), supports the assumption of a massive vegetation change in the vicinity of Lake Khamra after the 1950CE fire event. Furthermore, *Cyperaceae* have the capability to promptly establish in recently disturbed and deforested regions, as after a wildfire, beside growing on wet areas (Glückler et al. 2021 and references therein).

The lake-internal proxies also show a distinct shift at the time of  $\delta^{18}\text{O}_{\text{diatom}}$  maximum. Assuming that a severe fire had suddenly led to an opening of previously dense forest vegetation in the catchment, the affected area, especially the soil cover, would likely become more vulnerable to erosion from rain and snowmelt flowing into the lake. Even years after the fire event, the loss of vegetation cover could cause an altered input into the lake, in line with consistently above mean TIC values since the 1950s (Fig. 5). Additionally, the first peak in THg around 1960CE

(Fig. 5) might be related to changed conditions in the catchment area. Anthropogenic mercury inputs from increasing industrial combustion, transported by air as discussed in Sect. 5.3., is likely the main Hg source. Mercury can not only be released into the air from burning plant material (Driscoll et al., 2013), but can also accumulate in burned soils where it could subsequently be transported to the lake by erosion (Burke et al., 2010). For the first time within the Lake Khamra record, the mercury accumulation rates rise above the mean ( $26.6 \mu\text{g m}^{-2} \text{a}^{-1}$ ) between 1930CE and 1950CE. However, since the increase in accumulation rate is rather small, we assume the main Hg accumulation still is linked to the atmospheric Hg deposition from anthropogenic sources. Even though, z-scores of the  $\delta^{18}\text{O}_{\text{diatom}}$  record are less pronounced as in phase II, we identify a similar temporal correspondence between a charcoal peak in the early 1800s (Glückler et al., 2021) and elevated  $\delta^{18}\text{O}_{\text{diatom}}$  values in phase IV (Fig. 7). Hydroclimatic anomalies such as prolonged dry periods, which are mainly due to a deficit of winter precipitation, form the basis for enhanced forest fire activity in this area. This hydroclimatic variability is reflected in the diatom isotope record of Lake Khamra, which agrees well with the regional reconstruction of forest fires.

## 6 Conclusions

The presented  $\delta^{18}\text{O}_{\text{diatom}}$  record of Lake Khamra provides a valuable sub-decadal hydroclimate proxy record spanning from about 1790CE to 2015CE for the understudied area of south-west Yakutia in Eastern Siberia. For  
785 the period of meteorological measurements since the 1930s, we could exclude air temperature as main driving  
factor of the variability of the  $\delta^{18}\text{O}_{\text{diatom}}$  record of Lake Khamra. Instead,  $\delta^{18}\text{O}_{\text{diatom}}$  is linked to seasonal precipitation  
changes in the region, especially to variations in early winter precipitation that enter the lake as isotopically  
depleted snowmelt water. An overall depletion of  $\delta^{18}\text{O}_{\text{diatom}}$  since the 1950s is interpreted as an increase in winter  
precipitation in the area positively correlated with a winter NAO index. Prior to meteorological recordings, the  
790  $\delta^{18}\text{O}_{\text{diatom}}$  signal also appears to be little influenced by air temperature or solar insolation. The comparison with  
available palaeoclimate proxy records and other high-resolution  $\delta^{18}\text{O}_{\text{diatom}}$  records of the Northern Hemisphere  
support the  $\delta^{18}\text{O}_{\text{diatom}}$  record of Lake Khamra as a valuable hydroclimate proxy, especially for winter precipitation  
shifts.

Hydroclimatic anomalies are interpreted within the Lake Khamra  $\delta^{18}\text{O}_{\text{diatom}}$  record as dry periods likely caused by  
795 reduced winter precipitation leading to enriched  $\delta^{18}\text{O}_{\text{diatom}}$  values at the onset of the 19<sup>th</sup> century and especially in  
the 1950s, the latter is confirmed by meteorological data. These two dry periods overlap with reconstructed  
charcoal maxima, and serve as a potential explanation for high fire activity in the area despite rather cool  
temperatures, especially in times of an insolation minimum around 1800CE. This highlights that the reconstruction  
of hydroclimate conditions is highly valuable to better understand climatic drivers of past fire activity.

800 Nearly synchronous with the peak of  $\delta^{18}\text{O}_{\text{diatom}}$  around 1950CE, we detected a significant increase in mercury  
levels, which is mainly attributed to human air pollution, despite the remote location of Lake Khamra.

## Appendices

### Appendix A

805 **Table A1. Main geochemical characteristics and isotopic signature of diatom samples from Lake Khamra. The purity of the sample material has been determined by EDS. SiO<sub>2</sub> content ranges between 96.1 and 98.7%, Al<sub>2</sub>O<sub>3</sub> content between 0.4 and 0.7%. Mean δ<sup>18</sup>O<sub>diatom</sub> values (Diatom δ<sup>18</sup>O<sub>mean</sub>), calculated contamination (%) and δ<sup>18</sup>O values corrected for contamination (Diatom δ<sup>18</sup>O<sub>corrected</sub>) are given.**

Sample ID	Depth sed top (m)	Depth sed bottom (m)	Age (CE)	SiO <sub>2</sub> (%)	Al <sub>2</sub> O <sub>3</sub> (%)	Na <sub>2</sub> O (%)	MgO (%)	K <sub>2</sub> O (%)	CaO (%)	FeO (%)	total (%)	Diatom δ <sup>18</sup> O mean (% vs. SMOW)	Diatom δ <sup>18</sup> O std dev (±)	Repl (#)	Contamination (%)	Diatom δ <sup>18</sup> O corrected (% vs. SMOW)
EN18232-1-01	0.00	0.01	2015	96.59	0.44	2.55	0.11	0.12	0.08	0.19	100.08	21.29	0.17	2	3.85	21.50
EN18232-1-02	0.01	0.02	2009	96.75	0.46	2.40	0.07	0.12	0.06	0.15	100.01	21.29	0.26	3	4.03	21.50
EN18232-1-03	0.02	0.03	2000	97.42	0.46	1.73	0.06	0.07	0.07	0.20	100.00	20.65	0.17	2	4.06	20.84
EN18232-1-04	0.03	0.04	1990	96.54	0.64	2.33	0.04	0.16	0.04	0.25	100.01	21.46	0.20	2	5.65	21.78
EN18232-1-05	0.04	0.05	1980	97.07	0.49	2.04	0.06	0.10	0.07	0.19	100.01	21.72	0.24	3	4.31	21.97
EN18232-1-06	0.05	0.06	1970	96.05	0.55	2.97	0.11	0.14	0.06	0.17	100.04	21.80	0.21	2	4.84	22.09
EN18232-1-07	0.06	0.07	1961	96.47	0.69	2.43	0.06	0.09	0.07	0.21	100.02	22.08	0.06	2	6.14	22.47
EN18232-1-08	0.07	0.08	1953	97.13	0.52	1.98	0.05	0.12	0.06	0.16	100.01	23.11	0.22	2	4.59	23.45
EN18232-1-09	0.08	0.09	1947	96.45	0.55	2.58	0.08	0.13	0.07	0.19	100.04	22.26	0.09	2	4.85	22.57
EN18232-1-10	0.09	0.10	1941	98.60	0.54	0.44	0.06	0.05	0.11	0.21	100.00	20.39	0.14	2	4.77	20.60
EN18232-1-11	0.10	0.11	1936	96.70	0.57	2.25	0.07	0.15	0.07	0.19	100.00	22.40	0.11	2	5.08	22.73
EN18232-1-12	0.11	0.12	1930	97.72	0.69	1.09	0.08	0.11	0.08	0.24	100.00	21.30	0.26	2	6.08	21.63
EN18232-1-13	0.12	0.13	1925	98.66	0.50	0.46	0.04	0.04	0.10	0.22	100.00	21.22	0.10	2	4.38	21.46
EN18232-1-14	0.13	0.14	1920	97.07	0.51	2.05	0.03	0.11	0.06	0.18	100.00	21.66	0.13	2	4.47	21.92
EN18232-1-15	0.14	0.15	1915	97.90	0.70	0.94	0.06	0.11	0.08	0.21	100.00	20.32	0.21	2	6.16	20.59
EN18232-1-16	0.15	0.16	1909	97.45	0.43	1.77	0.05	0.08	0.08	0.17	100.02	21.56	0.16	2	3.76	21.78
EN18232-1-17	0.16	0.17	1904	96.57	0.44	2.65	0.07	0.09	0.07	0.14	100.03	21.54	0.05	2	3.85	21.76
EN18232-1-18	0.17	0.18	1899	97.37	0.43	1.77	0.06	0.06	0.09	0.25	100.04	20.76	0.21	2	3.82	20.94
EN18232-1-19	0.18	0.19	1894	98.40	0.56	0.71	0.04	0.04	0.09	0.18	100.01	20.89	0.02	2	4.91	21.13
EN18232-1-20	0.19	0.20	1889	96.25	0.50	2.92	0.07	0.10	0.07	0.15	100.05	22.03	0.14	2	4.43	22.31
EN18232-1-21	0.20	0.21	1884	97.24	0.49	2.00	0.06	0.03	0.06	0.15	100.01	21.45	0.24	2	4.29	21.69
EN18232-1-22	0.21	0.22	1879	97.16	0.42	2.15	0.05	0.06	0.07	0.13	100.03	20.81	0.05	2	3.69	20.99
EN18232-1-23	0.22	0.23	1874	98.53	0.46	0.74	0.04	0.02	0.08	0.15	100.03	20.40	0.26	3	4.09	20.59
EN18232-1-24	0.23	0.24	1869	97.31	0.53	1.85	0.05	0.04	0.07	0.17	100.02	21.42	0.15	2	4.71	21.68
EN18232-1-25	0.24	0.25	1864	97.63	0.71	1.19	0.09	0.10	0.09	0.19	99.99	20.99	0.06	2	6.32	21.32
EN18232-1-26	0.25	0.26	1859	97.82	0.49	1.42	0.07	0.02	0.07	0.14	100.02	21.09	0.16	2	4.29	21.31
EN18232-1-27	0.26	0.27	1853	97.86	0.44	1.45	0.04	0.02	0.04	0.17	100.01	21.33	0.22	2	3.87	21.54
EN18232-1-28	0.27	0.28	1848	98.37	0.46	0.84	0.04	0.02	0.09	0.19	100.01	20.94	0.10	2	4.07	21.14
EN18232-1-29	0.28	0.29	1843	97.25	0.50	1.93	0.04	0.03	0.10	0.19	100.02	21.58	0.15	2	4.46	21.84
EN18232-1-30	0.29	0.30	1838	97.91	0.66	1.06	0.06	0.09	0.04	0.18	100.00	20.96	0.15	2	5.84	21.26
EN18232-1-31	0.30	0.31	1833	97.55	0.54	1.54	0.06	0.05	0.10	0.18	100.01	21.12	0.22	2	4.74	21.37
EN18232-1-32	0.31	0.32	1828	97.31	0.39	1.96	0.07	0.03	0.08	0.18	100.01	22.00	0.05	2	3.44	22.21
EN18232-1-33	0.32	0.33	1823	97.19	0.51	2.01	0.05	0.03	0.07	0.17	100.02	22.29	0.01	2	4.49	22.58
EN18232-1-34	0.33	0.34	1818	97.62	0.52	1.53	0.03	0.04	0.09	0.19	100.02	22.06	0.01	2	4.60	22.34

EN18232-1-35	0.34	0.35	1813	97.88	0.54	1.21	0.05	0.08	0.08	0.17	100.01	21.37	0.01	2	4.77	21.63
EN18232-1-36	0.35	0.36	1808	97.47	0.61	1.53	0.10	0.04	0.09	0.22	100.05	21.98	0.19	2	5.36	22.31
EN18232-1-37	0.36	0.37	1803	97.53	0.40	1.79	0.03	0.03	0.08	0.15	100.02	21.70	0.15	2	3.57	21.90
EN18232-1-38	0.37	0.38	1798	97.79	0.53	1.34	0.05	0.04	0.10	0.18	100.02	21.71	0.03	2	4.69	21.99
EN18232-1-39	0.38	0.39	1793	98.10	0.57	1.02	0.04	0.03	0.08	0.17	100.02	21.99	0.26	2	5.05	22.30

---

810

### **Data availability**

The datasets used in this study, including water isotope data,  $^{14}\text{C}$  and  $^{210}\text{Pb}$ – $^{137}\text{Cs}$  dates, mercury, total inorganic carbon and the Khamra  $\delta^{18}\text{O}_{\text{diatom}}$  record are available via PANGAEA, Stieg et al. (2024).

### 815 **Authors contributions**

AS, HM, BKB and UH designed the research project. BKB, UH and LP conducted fieldwork and received the sediment core and water samples in 2018 and 2020. AS processed and analysed the sediment samples in the lab, and together with HM interpreted the diatom and water isotope datasets. AS coordinated the sediment dating, did the age-depth modelling. JS supervised mercury and inorganic carbon analysis and helped interpreting these  
820 proxies. AS, HM and BKB structured the manuscript. AS produced all figures and tables and wrote the manuscript. All authors commented on drafts and have approved the final version.

### **Competing interests**

The authors declare that they have no conflict of interest.

825

### **Disclaimer**

Maps throughout this article were created using the Free and Open Source QGIS Geographic Information System. QGIS.org, Version 3.12, 2023 and the plugin ‘Globe Builder’ including OpenStreetMap data. This plugin is licenced with GNU General Public License, version 2. This plugin uses OpenStreetMap Nominatim geocoding  
830 API, © OpenStreetMap contributors 2023. Distributed under the Open Data Commons Open Database License (ODbL) v1.0..

### **Acknowledgments**

We thank the teams of the ISOLAB Facility, the CarLa lab and the MICADAS radiocarbon laboratory of AWI.  
835 We would further like to thank Ramesh Glückler for his help sampling the sediment core and for his expertise in regional wildfire reconstruction, as well as all participants of the joint German-Russian expedition in Yakutia 2018 and 2020 for their support. We thank the editor Bjørg Risebrobakken, and the referee Anson Mackay as well as an anonymous reviewer for their valuable assessment of the manuscript and for their helpful comments to improve our work.

840

### **Funding details**

Amelie Stieg is funded by AWI INSPIRES (International Science Program for Integrative Research in Earth Systems). The article processing charges for this open-access publication were covered by the Alfred Wegener Institute, Helmholtz Centre for Polar and Marine Research (AWI).

## 845 7 References

- Appleby, P. G., Nolan, P. J., Gifford, D. W., Godfrey, M. J., Oldfield, F., Anderson, N. J., and Battarbee, R. W.: <sup>210</sup>Pb dating by low background gamma counting, *Hydrobiologia*, 143, 21-27, 10.1007/bf00026640, 1986.
- Bailey, H., Hubbard, A., Klein, E. S., Mustonen, K.-R., Akers, P. D., Marttila, H., and Welker, J. M.: Arctic sea-ice loss fuels extreme European snowfall, *Nature Geoscience*, 14, 283-288, 10.1038/s41561-021-00719-y, 2021.
- 850 Bintanja, R.: The impact of Arctic warming on increased rainfall, *Sci Rep*, 8, 16001, 10.1038/s41598-018-34450-3, 2018.
- Bintanja, R. and Selten, F. M.: Future increases in Arctic precipitation linked to local evaporation and sea-ice retreat, *Nature*, 509, 479-482, 10.1038/nature13259, 2014.
- Biskaborn, B. K., Herzschuh, U., Bolshiyarov, D., Savelieva, L., and Diekmann, B.: Environmental variability in northeastern Siberia during the last ~ 13,300 yr inferred from lake diatoms and sediment–geochemical parameters, *Palaeogeography, Palaeoclimatology, Palaeoecology*, 329-330, 22-36, 10.1016/j.palaeo.2012.02.003, 2012.
- 855 Biskaborn, B. K., Bolshiyarov, Dmitry, Grigoriev, Mikhail N. , Morgenstern, Anne , Pestryakova, Luidmila A. , Tsibizov, Leonid and Dill, Antonia: Russian-German Cooperation: Expeditions to Siberia in 2020, *Berichte zur Polar- und Meeresforschung = Reports on polar and marine research*, Alfred Wegener Institute for Polar and
- 860 Marine Research, Bremerhaven, 81, 10.48433/BzPM\_0756\_2021, 2021a.
- Biskaborn, B. K., Narancic, B., Stoof-Leichsenring, K. R., Pestryakova, L. A., Appleby, P. G., Piliposian, G. T., and Diekmann, B.: Effects of climate change and industrialization on Lake Bolshoe Toko, eastern Siberia, *Journal of Paleolimnology*, 65, 335-352, 10.1007/s10933-021-00175-z, 2021b.
- Biskaborn, B. K., Forster, A., Pfalz, G., Pestryakova, L. A., Stoof-Leichsenring, K., Strauss, J., Kröger, T., and Herzschuh, U.: Diatom responses and geochemical feedbacks to environmental changes at Lake Rauchaugytyn (Far East Russian Arctic), *Biogeosciences*, 20, 1691-1712, 10.5194/bg-20-1691-2023, 2023.
- 865 Björck, S. and Wohlfarth, B.: *<sup>14</sup>C Chronostratigraphic Techniques in Paleolimnology*, in: *Tracking Environmental Change Using Lake Sediments: Basin Analysis, Coring, and Chronological Techniques*, edited by: Last, W. M., and Smol, J. P., Springer Netherlands, Dordrecht, 205-245, 10.1007/0-306-47669-X\_10, 978-0-306-47669-3, 2001.
- 870 Blaauw, M. and Christen, J. A.: Flexible paleoclimate age-depth models using an autoregressive gamma process, *Bayesian Analysis*, 6, 10.1214/11-ba618, 2011.
- Bowen, G. J.: The Online Isotopes in Precipitation Calculator, version OIPC3.1: <http://www.waterisotopes.org>, last access: 18 October 2023.
- 875 Bowen, G. J. and Revenaugh, J.: Interpolating the isotopic composition of modern meteoric precipitation, *Water Resour Res*, 39, <https://doi.org/10.1029/2003WR002086>, 2003.
- Bowen, G. J., Wassenaar, L. I., and Hobson, K. A.: Global application of stable hydrogen and oxygen isotopes to wildlife forensics, *Oecologia*, 143, 337-348, 10.1007/s00442-004-1813-y, 2005.
- 880 Bradley, R. S.: *Paleoclimatology: Reconstructing Climates of the Quaternary*, 3rd ed, Academic Press, San Diego [u.a.] 9780123869135, 2015.
- Brewer, T. S., Leng, M. J., Mackay, A. W., Lamb, A. L., Tyler, J. J., and Marsh, N. G.: Unravelling contamination signals in biogenic silica oxygen isotope composition: the role of major and trace element geochemistry, *Journal of Quaternary Science*, 23, 321-330, 10.1002/jqs.1171, 2008.
- 885 Broadman, E., Kaufman, D. S., Henderson, A. C. G., Berg, E. E., Anderson, R. S., Leng, M. J., Stahnke, S. A., and Muñoz, S. E.: Multi-proxy evidence for millennial-scale changes in North Pacific Holocene hydroclimate from the Kenai Peninsula lowlands, south-central Alaska, *Quaternary Science Reviews*, 241, 10.1016/j.quascirev.2020.106420, 2020.
- Broadman, E., Kaufman, D. S., Anderson, R. S., Bogle, S., Ford, M., Fortin, D., Henderson, A. C. G., Lacey, J. H., Leng, M. J., McKay, N. P., and Muñoz, S. E.: Reconstructing postglacial hydrologic and environmental change in the eastern Kenai Peninsula lowlands using proxy data and mass balance modeling, *Quaternary Research*, 107, 1-26, <https://doi.org/10.1017/qua.2021.75>, 2022.
- 890 Brown, J., Ferrians Jr, O. J., Heginbottom, J. A., and Melnikov, E. S.: Circum-Arctic map of permafrost and ground-ice conditions, Report 45, 10.3133/cp45, 1997.
- 895 Bulygina, O. N., Razuvaev, V. N., and Korshunova, N. N.: Changes in snow cover over Northern Eurasia in the last few decades, *Environmental Research Letters*, 4, 10.1088/1748-9326/4/4/045026, 2009.



- Burke, M. P., Hogue, T. S., Ferreira, M., Mendez, C. B., Navarro, B., Lopez, S., and Jay, J. A.: The Effect of Wildfire on Soil Mercury Concentrations in Southern California Watersheds, *Water Air Soil Pollut*, 212, 369-385, 10.1007/s11270-010-0351-y, 2010.
- 900 Chaplignin, B., Narancic, B., Meyer, H., and Pienitz, R.: Paleo-environmental gateways in the eastern Canadian arctic - Recent isotope hydrology and diatom oxygen isotopes from Nettilling Lake, Baffin Island, Canada, *Quaternary Science Reviews*, 147, 379-390, 10.1016/j.quascirev.2016.03.028, 2016.
- Chaplignin, B., Meyer, H., Bryan, A., Snyder, J., and Kemnitz, H.: Assessment of purification and contamination correction methods for analysing the oxygen isotope composition from biogenic silica, *Chemical Geology*, 300-301, 185-199, 10.1016/j.chemgeo.2012.01.004, 2012a.
- 905 Chaplignin, B., Meyer, H., Swann, G. E. A., Meyer-Jacob, C., and Hubberten, H. W.: A 250 ka oxygen isotope record from diatoms at Lake El'gygytgyn, far east Russian Arctic, *Clim Past*, 8, 1621-1636, 10.5194/cp-8-1621-2012, 2012b.
- Chaplignin, B., Meyer, H., Friedrichsen, H., Marent, A., Sohns, E., and Hubberten, H. W.: A high-performance, safer and semi-automated approach for the  $\delta^{18}\text{O}$  analysis of diatom silica and new methods for removing exchangeable oxygen, *Rapid Commun Mass Spectrom*, 24, 2655-2664, 10.1002/rcm.4689, 2010.
- 910 Chaplignin, B., Leng, M. J., Webb, E., Alexandre, A., Dodd, J. P., Ijiri, A., Lücke, A., Shemesh, A., Abelman, A., Herzschuh, U., Longstaffe, F. J., Meyer, H., Moschen, R., Okazaki, Y., Rees, N. H., Sharp, Z. D., Sloane, H. J., Sonzogni, C., Swann, G. E. A., Sylvestre, F., Tyler, J. J., and Yam, R.: Inter-laboratory comparison of oxygen isotope compositions from biogenic silica, *Geochim Cosmochim Acta*, 75, 7242-7256, 10.1016/j.gca.2011.08.011, 2011.
- 915 Geologic map of Yakutia P-48,49, 1 : 1000000, VSEGEI, Leningrad: <http://www.geokniga.org/sites/geokniga/>, last access: 11.11.2022.
- Churakova Sidorova, O. V., Siegwolf, R. T. W., Fonti, M. V., Vaganov, E. A., and Saurer, M.: Spring arctic oscillation as a trigger of summer drought in Siberian subarctic over the past 1494 years, *Scientific Reports*, 11, 19010, 10.1038/s41598-021-97911-2, 2021.
- 920 Chylek, P., Folland, C., Klett, J. D., Wang, M., Hengartner, N., Lesins, G., and Dubey, M. K.: Annual Mean Arctic Amplification 1970–2020: Observed and Simulated by CMIP6 Climate Models, *Geophysical Research Letters*, 49, 10.1029/2022gl099371, 2022.
- 925 Ciavarella, A., Cotterill, D., Stott, P., Kew, S., Philip, S., van Oldenborgh, G. J., Skalevag, A., Lorenz, P., Robin, Y., Otto, F., Hauser, M., Seneviratne, S. I., Lehner, F., and Zolina, O.: Prolonged Siberian heat of 2020 almost impossible without human influence, *Clim Change*, 166, 9, 10.1007/s10584-021-03052-w, 2021.
- Clayton, R. N. and Mayeda, T. K.: The use of bromine pentafluoride in the extraction of oxygen from oxides and silicates for isotopic analysis, *Geochim Cosmochim Acta*, 27, 43-52, 10.1016/0016-7037(63)90071-1, 1963.
- 930 Coddington, O., Lean, J. L., Lindholm, D., Pilewskie, P., Snow, M., and Program, N. C.: NOAA Climate Data Record (CDR) of Total Solar Irradiance (TSI), NRLTSI Version 2 [dataset], 10.7289/V55B00C1 2015.
- Cohen, A. S.: *Paleolimnology: The history and evolution of lake systems*, Oxford University Press, New York, 0-19-513353-6, 2003.
- 935 Collow, A. B. M., Thomas, N. P., Bosilovich, M. G., Lim, Y.-K., Schubert, S. D., and Koster, R. D.: Seasonal Variability in the Mechanisms behind the 2020 Siberian Heatwaves, *Journal of Climate*, 35, 3075-3090, 10.1175/jcli-d-21-0432.1, 2022.
- Colman, S. M., Jones, G. A., Rubin, M., King, J. W., Peck, J. A., and Orem, W. H.: AMS radiocarbon analyses from Lake Baikal, Siberia: Challenges of dating sediments from a large, oligotrophic lake, *Quaternary Science Reviews*, 15, 669-684, 10.1016/0277-3791(96)00027-3, 1996.
- 940 Craig, H.: Isotopic Variations in Meteoric Waters, *Science*, 133, 1702-1703, 10.1126/science.133.3465.1702, 1961.
- Dansgaard, W.: Stable isotopes in precipitation, *Tellus A: Dynamic Meteorology and Oceanography*, 16, 10.3402/tellusa.v16i4.8993, 1964.
- 945 Dodd, J. P. and Sharp, Z. D.: A laser fluorination method for oxygen isotope analysis of biogenic silica and a new oxygen isotope calibration of modern diatoms in freshwater environments, *Geochim Cosmochim Acta*, 74, 1381-1390, <https://doi.org/10.1016/j.gca.2009.11.023>, 2010.
- Durre, I., Menne, M. J., and Vose, R. S.: Strategies for evaluating quality assurance procedures, *Journal of Applied Meteorology and Climatology*, 47, 1785-1791, 10.1175/2007jamc1706.1, 2008.

- Driscoll, C. T., Mason, R. P., Chan, H. M., Jacob, D. J., and Pirrone, N.: Mercury as a Global Pollutant: Sources, Pathways, and Effects, *Environmental Science & Technology*, 47, 4967-4983, 10.1021/es305071v, 2013.
- 950 Eckhardt, S., Pisso, I., Evangeliou, N., Zwaafink, C. G., Plach, A., McConnell, J. R., Sigl, M., Ruppel, M., Zdanowicz, C., Lim, S., Chellman, N., Opel, T., Meyer, H., Steffensen, J. P., Schwikowski, M., and Stohl, A.: Revised historical Northern Hemisphere black carbon emissions based on inverse modeling of ice core records, *Nat Commun*, 14, 271, 10.1038/s41467-022-35660-0, 2023.
- Fedorov, A., Vasilyev, N., Torgovkin, Y., Shestakova, A., Varlamov, S., Zheleznyak, M., Shepelev, V.,  
 955 Konstantinov, P., Kalinicheva, S., Basharin, N., Makarov, V., Ugarov, I., Efremov, P., Argunov, R., Egorova, L., Samsonova, V., Shepelev, A., Vasiliev, A., Ivanova, R., Galanin, A., Lytkin, V., Kuzmin, G., and Kunitzky, V.: Permafrost-Landscape Map of the Republic of Sakha (Yakutia) on a Scale 1:1,500,000, *Geosciences*, 8, 10.3390/geosciences8120465, 2018.
- Ghatak, D., Frei, A., Gong, G., Stroeve, J., and Robinson, D.: On the emergence of an Arctic amplification signal  
 960 in terrestrial Arctic snow extent, *Journal of Geophysical Research: Atmospheres*, 115, 10.1029/2010jd014007, 2010.
- Ghatak, D., Deser, C., Frei, A., Gong, G., Phillips, A., Robinson, D. A., and Stroeve, J.: Simulated Siberian snow cover response to observed Arctic sea ice loss, 1979-2008, *Journal of Geophysical Research: Atmospheres*, 117, n/a-n/a, 10.1029/2012jd018047, 2012.
- 965 Gibson, C. E., Anderson, N. J., and Haworth, E. Y.: *Aulacoseira subarctica*: taxonomy, physiology, ecology and palaeoecology, *European Journal of Phycology*, 38, 83-101, 10.1080/0967026031000094102, 2003.
- Giglio, L., Boschetti, L., Roy, D. P., Humber, M. L., and Justice, C. O.: The Collection 6 MODIS burned area mapping algorithm and product, *Remote Sens Environ*, 217, 72-85, 10.1016/j.rse.2018.08.005, 2018.
- Glückler, R., Herzschuh, U., Kruse, S., Andreev, A., Vyse, S. A., Winkler, B., Biskaborn, B. K., Pestryakova, L.,  
 970 and Dietze, E.: Wildfire history of the boreal forest of south-western Yakutia (Siberia) over the last two millennia documented by a lake-sediment charcoal record, *Biogeosciences*, 18, 4185-4209, 10.5194/bg-18-4185-2021, 2021.
- Gorokhov, A. N. and Fedorov, A. N.: Current Trends in Climate Change in Yakutia, *Geography and Natural Resources*, 39, 153-161, 10.1134/s1875372818020087, 2018.
- Hansen, M. C., Potapov, P. V., Moore, R., Hancher, M., Turubanova, S. A., Tyukavina, A., Thau, D., Stehman, S.  
 975 V., Goetz, S. J., Loveland, T. R., Kommareddy, A., Egorov, A., Chini, L., Justice, C. O., and Townshend, J. R.: High-resolution global maps of 21st-century forest cover change, *Science*, 342, 850-853, 10.1126/science.1244693, 2013.
- Hurrell, J. W.: Decadal trends in the north atlantic oscillation: regional temperatures and precipitation, *Science*, 269, 676-679, 10.1126/science.269.5224.676, 1995.
- 980 Hurrell, J. W. and Deser, C.: North Atlantic climate variability: The role of the North Atlantic Oscillation, *Journal of Marine Systems*, 79, 231-244, 10.1016/j.jmarsys.2009.11.002, 2010.
- IAEA/WMO: Global Network for Isotopes in Precipitation. The GNIP Database. Accessible at: <https://nucleus.iaea.org/wiser> [dataset], 2023.
- Jonsson, C. E., Rosqvist, G. C., Leng, M. J., Bigler, C., Bergman, J., Tillman, P. K., and Sloane, H. J.: High-  
 985 resolution diatom  $\delta^{18}O$  records, from the last 150 years, reflecting changes in amount of winter precipitation in two sub-Arctic high-altitude lakes in the Swedish Scandes, *Journal of Quaternary Science*, 25, 918-930, <https://doi.org/10.1002/jqs.1372>, 2010.
- Kandlbauer, J., Hopcroft, P. O., Valdes, P. J., and Sparks, R. S. J.: Climate and carbon cycle response to the 1815  
 990 Tambora volcanic eruption, *Journal of Geophysical Research: Atmospheres*, 118, 12,497-412,507, 10.1002/2013jd019767, 2013.
- Kirillina, K., Shvetsov, E. G., Protopopova, V. V., Thiesmeyer, L., and Yan, W.: Consideration of anthropogenic factors in boreal forest fire regime changes during rapid socio-economic development: case study of forestry districts with increasing burnt area in the Sakha Republic, Russia, *Environmental Research Letters*, 15, 10.1088/1748-9326/ab6c6e, 2020.
- 995 Klein Tank, A. M. G., Wijngaard, J. B., Können, G. P., Böhm, R., Demarée, G., Gocheva, A., Mileta, M., Pashiardis, S., Hejkrlik, L., Kern-Hansen, C., Heino, R., Bessemoulin, P., Müller-Westermeier, G., Tzanakou, M., Szalai, S., Pálsdóttir, T., Fitzgerald, D., Rubin, S., Capaldo, M., Maugeri, M., Leitass, A., Bukantis, A., Aberfeld, R., van Engelen, A. F. V., Forland, E., Miletus, M., Coelho, F., Mares, C., Razuvaev, V., Nieplova, E., Cegnar, T., Antonio López, J., Dahlström, B., Moberg, A., Kirchhofer, W., Ceylan, A., Pachaliuk, O., Alexander, L. V., and

- 1000 Petrovic, P.: Daily dataset of 20th-century surface air temperature and precipitation series for the European Climate Assessment, *International Journal of Climatology*, 22, 1441-1453, 10.1002/joc.773, 2002.
- Kostrova, S. S., Meyer, H., Chaplignin, B., Bezrukova, E. V., Tarasov, P. E., and Kuz'min, M. I.: Reconstruction of the Holocene climate of Transbaikalia: Evidence from the oxygen isotope analysis of fossil diatoms from Kotokel Lake, *Doklady Earth Sciences*, 451, 732-736, 10.1134/S1028334x13070039, 2013a.
- 1005 Kostrova, S. S., Meyer, H., Chaplignin, B., Kossler, A., Bezrukova, E. V., and Tarasov, P. E.: Holocene oxygen isotope record of diatoms from Lake Kotokel (southern Siberia, Russia) and its palaeoclimatic implications, *Quatern Int*, 290, 21-34, 10.1016/j.quaint.2012.05.011, 2013b.
- Kostrova, S. S., Meyer, H., Chaplignin, B., Tarasov, P. E., and Bezrukova, E. V.: The last glacial maximum and late glacial environmental and climate dynamics in the Baikal region inferred from an oxygen isotope record of lacustrine diatom silica, *Quatern Int*, 348, 25-36, 10.1016/j.quaint.2014.07.034, 2014.
- 1010 Kostrova, S. S., Meyer, H., Bailey, H. L., Ludikova, A. V., Gromig, R., Kuhn, G., Shibaev, Y. A., Kozachek, A. V., Ekaykin, A. A., and Chaplignin, B.: Holocene hydrological variability of Lake Ladoga, northwest Russia, as inferred from diatom oxygen isotopes, *Boreas*, 48, 361-376, 10.1111/bor.12385, 2019.
- Kostrova, S. S., Meyer, H., Fernandoy, F., Werner, M., and Tarasov, P. E.: Moisture origin and stable isotope characteristics of precipitation in southeast Siberia, *Hydrological Processes*, 34, 51-67, 10.1002/hyp.13571, 2020.
- Kostrova, S. S., Biskaborn, B. K., Pestryakova, L. A., Fernandoy, F., Lenz, M. M., and Meyer, H.: Climate and environmental changes of the Lateglacial transition and Holocene in northeastern Siberia: Evidence from diatom oxygen isotopes and assemblage composition at Lake Emanda, *Quaternary Science Reviews*, 259, 10.1016/j.quascirev.2021.106905, 2021.
- 1020 Kruse, S., Bolshiyarov, D., Grigoriev, M. N., Morgenstern, A., Pestryakova, L., Tsibizov, L., and Udke, A.: Russian-German Cooperation: Expeditions to Siberia in 2018, [https://doi.org/10.2312/BzPM\\_0734\\_2019](https://doi.org/10.2312/BzPM_0734_2019), 2019.
- Kurita, N., Yoshida, N., Inoue, G., and Chayanova, E. A.: Modern isotope climatology of Russia: A first assessment, *Journal of Geophysical Research: Atmospheres*, 109, n/a-n/a, 10.1029/2003jd003404, 2004.
- Laing, T. E. and Smol, J. P.: Late Holocene environmental changes inferred from diatoms in a lake on the western Taimyr Peninsula, northern Russia, *Journal of Paleolimnology*, 30, 231-247, 10.1023/A:1025561905506, 2003.
- 1025 Last, W. M., and Smol, J. P. (Eds.): *Tracking Environmental Change Using Lake Sediments. Volume 2: Physical and Geochemical Methods, Developments in Paleoenvironmental Research*, Springer Dordrecht, 10.1007/0-306-47670-3, 978-0-306-47670-9, 2001.
- Leclerc, A. J. and Labeyrie, L.: Temperature dependence of the oxygen isotopic fractionation between diatom silica and water, *Earth and Planetary Science Letters*, 84, 69-74, [https://doi.org/10.1016/0012-821X\(87\)90177-4](https://doi.org/10.1016/0012-821X(87)90177-4), 1987.
- Leng, M. J. and Barker, P. A.: A review of the oxygen isotope composition of lacustrine diatom silica for palaeoclimate reconstruction, *Earth-Science Reviews*, 75, 5-27, 10.1016/j.earscirev.2005.10.001, 2006.
- Leng, M. J. and Sloane, H. J.: Combined oxygen and silicon isotope analysis of biogenic silica, *Journal of Quaternary Science*, 23, 313-319, 10.1002/jqs.1177, 2008.
- 1035 Leng, M. J., Swann, G. E. A., Hodson, M. J., Tyler, J. J., Patwardhan, S. V., and Sloane, H. J.: The Potential use of Silicon Isotope Composition of Biogenic Silica as a Proxy for Environmental Change, *Silicon*, 1, 65-77, 10.1007/s12633-009-9014-2, 2009.
- Lenz, M. M., Andreev, A., Nazarova, L., Syrykh, L. S., Scheidt, S., Haflidason, H., Meyer, H., Brill, D., Wagner, B., Gromig, R., Lenz, M., Rolf, C., Kuhn, G., Fedorov, G., Svendsen, J. I., and Melles, M.: Climate, glacial and vegetation history of the polar Ural Mountains since c. 27 cal ka BP, inferred from a 54 m long sediment core from Lake Bolshoye Shchuchye, *Journal of Quaternary Science*, 37, 818-835, 10.1002/jqs.3400, 2021.
- Liu, Y., An, W., Wang, X., and Xu, C.: Moisture history in the Northeast China since 1750s reconstructed from tree-ring cellulose oxygen isotope, *Quatern Int*, 10.1016/j.quaint.2022.03.009, 2022.
- 1045 Mackay, A. W., Swann, G. E. A., Fagel, N., Fietz, S., Leng, M. J., Morley, D., Rioual, P., and Tarasov, P.: Hydrological instability during the Last Interglacial in central Asia: a new diatom oxygen isotope record from Lake Baikal, *Quaternary Science Reviews*, 66, 45-54, 10.1016/j.quascirev.2012.09.025, 2013.
- Manabe, S. and Stouffer, R. J.: Sensitivity of a global climate model to an increase of CO<sub>2</sub> concentration in the atmosphere, *Journal of Geophysical Research*, 85, 10.1029/JC085iC10p05529, 1980.
- 1050 Marshall, G. J.: Decadal Variability in the Impact of Atmospheric Circulation Patterns on the Winter Climate of Northern Russia, *Journal of Climate*, 34, 1005-1021, 10.1175/jcli-d-20-0566.1, 2021.

- McKay, N. P. and Kaufman, D. S.: An extended Arctic proxy temperature database for the past 2,000 years, *Sci Data*, 1, 140026, 10.1038/sdata.2014.26, 2014.
- 1055 Meister, P., Alexandre, A., Bailey, H., Barker, P., Biskaborn, B. K., Broadman, E., Cartier, R., Chaplignin, B., Couapel, M., Dean, J. R., Diekmann, B., Harding, P., Henderson, A. C. G., Hernandez, A., Herzsuh, U., Kostrova, S. S., Lacey, J., Leng, M. J., Lücke, A., Mackay, A. W., Magyari, E. K., Narancic, B., Porchier, C., Rosqvist, G., Shemesh, A., Sonzogni, C., Swann, G. E. A., Sylvestre, F., and Meyer, H.: A global compilation of diatom silica oxygen isotope records from lake sediment – trends, and implications for climate reconstruction, in review 2023, *Clim. Past Discuss.* [preprint], 1-44, <https://doi.org/10.5194/cp-2022-96>, 2023.
- 1060 Messenger, M. L., Lehner, B., Grill, G., Nedeva, I., and Schmitt, O.: Estimating the volume and age of water stored in global lakes using a geo-statistical approach, *Nat Commun*, 7, 13603, 10.1038/ncomms13603, 2016.
- Meyer, H., Schonicke, L., Wand, U., Hubberten, H. W., and Friedrichsen, H.: Isotope studies of hydrogen and oxygen in ground ice-experiences with the equilibration technique, *Isotopes Environ Health Stud*, 36, 133-149, 10.1080/10256010008032939, 2000.
- 1065 Meyer, H., Chaplignin, B., Hoff, U., Nazarova, L., and Diekmann, B.: Oxygen isotope composition of diatoms as Late Holocene climate proxy at Two-Yurts Lake, Central Kamchatka, Russia, *Global and Planetary Change*, 134, 118-128, 10.1016/j.gloplacha.2014.04.008, 2015.
- Meyer, H., Kostrova, S. S., Meister, P., Lenz, M. M., Kuhn, G., Nazarova, L., Syrykh, L. S., and Dvornikov, Y.: Lacustrine diatom oxygen isotopes as palaeo precipitation proxy - Holocene environmental and snowmelt variations recorded at Lake Bolshoye Shchuchye, Polar Urals, Russia, *Quaternary Science Reviews*, 290, 10.1016/j.quascirev.2022.107620, 2022.
- 1070 Miesner, T., Herzsuh, U., Pestryakova, L. A., Wieczorek, M., Zakharov, E. S., Kolmogorov, A. I., Davydova, P. V., and Kruse, S.: Forest structure and individual tree inventories of northeastern Siberia along climatic gradients, *Earth Syst. Sci. Data*, 14, 5695-5716, 10.5194/essd-14-5695-2022, 2022.
- 1075 Miller, G. H., Alley, R. B., Brigham-Grette, J., Fitzpatrick, J. J., Polyak, L., Serreze, M. C., and White, J. W. C.: Arctic amplification: can the past constrain the future?, *Quaternary Science Reviews*, 29, 1779-1790, 10.1016/j.quascirev.2010.02.008, 2010.
- Mock, C. J., Bartlein, P. J., and Anderson, P. M.: Atmospheric circulation patterns and spatial climatic variations in Beringia, *International Journal of Climatology*, 18, 1085-1104, 10.1002/(sici)1097-0088(199808)18:10<1085::Aid-joc305>3.0.Co;2-k, 1998.
- 1080 Mollenhauer, G., Grotheer, H., Gentz, T., Bonk, E., and Hefter, J.: Standard operation procedures and performance of the MICADAS radiocarbon laboratory at Alfred Wegener Institute (AWI), Germany, *Nuclear Instruments and Methods in Physics Research Section B: Beam Interactions with Materials and Atoms*, 496, 45-51, 10.1016/j.nimb.2021.03.016, 2021.
- 1085 Morley, D. W., Leng, M. J., Mackay, A. W., Sloane, H. J., Rioual, P., and Battarbee, R. W.: Cleaning of lake sediment samples for diatom oxygen isotope analysis, *Journal of Paleolimnology*, 31, 391-401, 10.1023/B:JOPL.0000021854.70714.6b, 2004.
- Moschen, R., Lücke, A., and Schleser, G. H.: Sensitivity of biogenic silica oxygen isotopes to changes in surface water temperature and palaeoclimatology, *Geophysical Research Letters*, 32, n/a-n/a, 10.1029/2004gl022167, 2005.
- 1090 Osborn, T. J.: Recent variations in the winter North Atlantic Oscillation, *Weather*, 61, 353-355, 10.1256/wea.190.06, 2006.
- Overland, J. E. and Wang, M.: The 2020 Siberian heat wave, *International Journal of Climatology*, 41, 10.1002/joc.6850, 2020.
- 1095 Pacyna, J. M., Travnikov, O., De Simone, F., Hedgecock, I. M., Sundseth, K., Pacyna, E. G., Steenhuisen, F., Pirrone, N., Munthe, J., and Kindbom, K.: Current and future levels of mercury atmospheric pollution on a global scale, *Atmos. Chem. Phys.*, 16, 12495-12511, 10.5194/acp-16-12495-2016, 2016.
- Pfalz, G., Diekmann, B., Freytag, J.-C., Syrykh, L., Subetto, D. A., and Biskaborn, B. K.: Improving age–depth relationships by using the LANDO (“Linked age and depth modeling”) model ensemble, *Geochronology*, 4, 269-295, 10.5194/gchron-4-269-2022, 2022.
- 1100 Philippsen, B.: The freshwater reservoir effect in radiocarbon dating, *Heritage Science*, 1, 10.1186/2050-7445-1-24, 2013.
- Previdi, M., Smith, K. L., and Polyani, L. M.: Arctic amplification of climate change: a review of underlying mechanisms, *Environmental Research Letters*, 16, 10.1088/1748-9326/ac1c29, 2021.

- 1105 Rantanen, M., Karpechko, A. Y., Lipponen, A., Nordling, K., Hyvärinen, O., Ruosteenoja, K., Vihma, T., and Laaksonen, A.: The Arctic has warmed nearly four times faster than the globe since 1979, *Communications Earth & Environment*, 3, 10.1038/s43247-022-00498-3, 2022.
- Roberts, S., Adams, J. K., Mackay, A. W., Swann, G. E. A., McGowan, S., Rose, N. L., Panizzo, V., Yang, H., Vologina, E., Sturm, M., and Shchetnikov, A. A.: Mercury loading within the Selenga River basin and Lake Baikal, Siberia, *Environ Pollut*, 259, 113814, 10.1016/j.envpol.2019.113814, 2020.
- 1110 Reimer, P. J., Austin, W. E. N., Bard, E., Bayliss, A., Blackwell, P. G., Bronk Ramsey, C., Butzin, M., Cheng, H., Edwards, R. L., Friedrich, M., Grootes, P. M., Guilderson, T. P., Hajdas, I., Heaton, T. J., Hogg, A. G., Hughen, K. A., Kromer, B., Manning, S. W., Muscheler, R., Palmer, J. G., Pearson, C., van der Plicht, J., Reimer, R. W., Richards, D. A., Scott, E. M., Southon, J. R., Turney, C. S. M., Wacker, L., Adolphi, F., Büntgen, U., Capano, M., Fahrni, S. M., Fogtmann-Schulz, A., Friedrich, R., Köhler, P., Kudsk, S., Miyake, F., Olsen, J., Reinig, F., Sakamoto, M., Sookdeo, A., and Talamo, S.: The IntCal20 Northern Hemisphere Radiocarbon Age Calibration Curve (0–55 cal kBP), *Radiocarbon*, 62, 725–757, 10.1017/rdc.2020.41, 2020.
- 1115 Rosqvist, G. C., Rietti-Shati, M., and Shemesh, A.: Late glacial to middle Holocene climatic record of lacustrine biogenic silica oxygen isotopes from a Southern Ocean island, *Geology*, 27, 967–970, Doi 10.1130/0091-7613(1999)027<0967:Lgtmhc>2.3.Co;2, 1999.
- 1120 Rosqvist, G. C., Leng, M. J., Goslar, T., Sloane, H. J., Bigler, C., Cunningham, L., Dadal, A., Bergman, J., Berntsson, A., Jonsson, C., and Wastegård, S.: Shifts in precipitation during the last millennium in northern Scandinavia from lacustrine isotope records, *Quaternary Science Reviews*, 66, 22–34, 10.1016/j.quascirev.2012.10.030, 2013.
- 1125 Rutkowski, C., Lenz, J., Lang, A., Wolter, J., Mothes, S., Reemtsma, T., Grosse, G., Ulrich, M., Fuchs, M., Schirrmeister, L., Fedorov, A., Grigoriev, M., Lantuit, H., and Strauss, J.: Mercury in sediment core samples from deep Siberian ice-rich permafrost, *Frontiers in Earth Science*, 9, 10.3389/feart.2021.718153, 2021.
- Sato, T., Nakamura, T., Iijima, Y., and Hiyama, T.: Enhanced Arctic moisture transport toward Siberia in autumn revealed by tagged moisture transport model experiment, *npj Climate and Atmospheric Science*, 5, 10.1038/s41612-022-00310-1, 2022.
- 1130 Scholten, R. C., Coumou, D., Luo, F., and Veraverbeke, S.: Early snowmelt and polar jet dynamics co-influence recent extreme Siberian fire seasons, *Science*, 378, 1005–1009, 10.1126/science.abn4419, 2022.
- Seneviratne, S. I., X. Zhang, M. Adnan, W. Badi, C. Dereczynski, A. Di Luca, S. Ghosh, I. Iskandar, J. Kossin, S. Lewis, F. Otto, I. Pinto, M. Satoh, S.M. Vicente-Serrano, M. Wehner, and Zho, B.: Weather and Climate Extreme Events in a Changing Climate, in: *Climate Change 2021: The Physical Science Basis. Contribution of Working Group I to the Sixth Assessment Report of the Intergovernmental Panel on Climate Change* [Masson-Delmotte, V., P. Zhai, A. Pirani, S.L. Connors, C. Péan, S. Berger, N. Caud, Y. Chen, L. Goldfarb, M.I. Gomis, M. Huang, K. Leitzell, E. Lonnoy, J.B.R. Matthews, T.K. Maycock, T. Waterfield, O. Yelekçi, R. Yu, and B. Zhou (eds.)], Cambridge University Press, Cambridge, United Kingdom and New York, NY, USA, 1513–1766, 10.1017/9781009157896.013, 2021.
- 1135 Shahgedanova, M.: Climate at present and in the historical past, *The physical geography of northern Eurasia*, 70–102, 2002.
- Shemesh, A. and Peteet, D.: Oxygen isotopes in fresh water biogenic opal - Northeastern US Alleröd-Younger Dryas temperature shift, *Geophysical Research Letters*, 25, 1935–1938, 10.1029/98gl01443, 1998.
- 1145 Shemesh, A., Rosqvist, G., Rietti-Shati, M., Rubensdotter, L., Bigler, C., Yam, R., and Karlén, W.: Holocene climatic change in Swedish Lapland inferred from an oxygen-isotope record of lacustrine biogenic silica, *The Holocene*, 11, 447–454, 10.1191/095968301678302887, 2001.
- Stenchikov, G., Delworth, T. L., Ramaswamy, V., Stouffer, R. J., Wittenberg, A., and Zeng, F.: Volcanic signals in oceans, *Journal of Geophysical Research*, 114, 10.1029/2008jd011673, 2009.
- 1150 Stieg, Amelie; Biskaborn, Boris K; Herzschuh, Ulrike; Strauss, Jens; Pestryakova, Luidmila A; Meyer, Hanno (2024): Sub-decadal diatom oxygen isotope record and biogeochemical data of the last 220 years (2015–1790CE) based on a sediment short core from Lake Khamra, Yakutia, Siberia. PANGAEA, <https://doi.org/10.1594/PANGAEA.962988>
- 1155 Stuiver, M. and Reimer, P. J.: A Computer Program for Radiocarbon Age Calibration, *Radiocarbon*, 28, 1022–1030, 10.1017/S0033822200060276, 1986.
- Stuiver, M. and Reimer, P. J.: Extended 14C Data Base and Revised CALIB 3.0 14C Age Calibration Program, *Radiocarbon*, 35, 215–230, 10.1017/S0033822200013904, 1993.

- Sun, C., Li, J., and Zhao, S.: Remote influence of Atlantic multidecadal variability on Siberian warm season precipitation, *Sci Rep*, 5, 16853, 10.1038/srep16853, 2015.
- 1160 Sundseth, K., Pacyna, J. M., Pacyna, E. G., Pirrone, N., and Thorne, R. J.: Global Sources and Pathways of Mercury in the Context of Human Health, *Int J Environ Res Public Health*, 14, 10.3390/ijerph14010105, 2017.
- Swann, G. E. A. and Leng, M. J.: A review of diatom  $\delta^{18}\text{O}$  in palaeoceanography, *Quaternary Science Reviews*, 28, 384-398, 10.1016/j.quascirev.2008.11.002, 2009.
- 1165 Swann, G. E. A., Leng, M. J., Juschus, O., Melles, M., Brigham-Grette, J., and Sloane, H. J.: A combined oxygen and silicon diatom isotope record of Late Quaternary change in Lake El'gygytyn, North East Siberia, *Quaternary Science Reviews*, 29, 774-786, 10.1016/j.quascirev.2009.11.024, 2010.
- Swann, G. E. A., Mackay, A. W., Vologina, E., Jones, M. D., Panizzo, V. N., Leng, M. J., Sloane, H. J., Snelling, A. M., and Sturm, M.: Lake Baikal isotope records of Holocene Central Asian precipitation, *Quaternary Science Reviews*, 189, 210-222, 10.1016/j.quascirev.2018.04.013, 2018.
- 1170 Tomshin, O. and Solovyev, V.: Features of the Extreme Fire Season of 2021 in Yakutia (Eastern Siberia) and Heavy Air Pollution Caused by Biomass Burning, *Remote Sensing*, 14, 10.3390/rs14194980, 2022.
- Trouet, V., Esper, J., Graham, N. E., Baker, A., Scourse, J. D., and Frank, D. C.: Persistent positive North Atlantic oscillation mode dominated the Medieval Climate Anomaly, *Science*, 324, 78-80, 10.1126/science.1166349, 2009.
- 1175 van Hardenbroek, M., Chakraborty, A., Davies, K. L., Harding, P., Heiri, O., Henderson, A. C. G., Holmes, J. A., Lasher, G. E., Leng, M. J., Panizzo, V. N., Roberts, L., Schilder, J., Trueman, C. N., and Wooller, M. J.: The stable isotope composition of organic and inorganic fossils in lake sediment records: Current understanding, challenges, and future directions, *Quaternary Science Reviews*, 196, 154-176, 10.1016/j.quascirev.2018.08.003, 2018.
- Vyse, S. A., Herzsuh, U., Andreev, A. A., Pestryakova, L. A., Diekmann, B., Armitage, S. J., and Biskaborn, B. K.: Geochemical and sedimentological responses of arctic glacial Lake Ilirney, chukotka (far east Russia) to palaeoenvironmental change since  $\sim 51.8$  ka BP, *Quaternary Science Reviews*, 247, 10.1016/j.quascirev.2020.106607, 2020.
- 1180 Wang, Q., Kim, D., Dionysiou, D. D., Sorial, G. A., and Timberlake, D.: Sources and remediation for mercury contamination in aquatic systems--a literature review, *Environ Pollut*, 131, 323-336, 10.1016/j.envpol.2004.01.010, 2004.
- 1185 Watanabe, T., Matsuyama, H., Kuzhevskaja, I., Nechepurenko, O., Chursin, V., and Zemtsov, V.: Long-Term Trends of Extreme Climate Indexes in the Southern Part of Siberia in Comparison with Those of Surrounding Regions, *Atmosphere*, 14, 10.3390/atmos14071131, 2023.
- Wegmann, M., Orsolini, Y., Vázquez, M., Gimeno, L., Nieto, R., Bulygina, O., Jaiser, R., Handorf, D., Rinke, A., Dethloff, K., Sterin, A., and Brönnimann, S.: Arctic moisture source for Eurasian snow cover variations in autumn, *Environmental Research Letters*, 10, 10.1088/1748-9326/10/5/054015, 2015.
- 1190 Wetterich, S., Herzsuh, U., Meyer, H., Pestryakova, L., Plessen, B., Lopez, C. M. L., and Schirrmeister, L.: Evaporation effects as reflected in freshwaters and ostracod calcite from modern environments in Central and Northeast Yakutia (East Siberia, Russia), *Hydrobiologia*, 614, 171-195, 10.1007/s10750-008-9505-y, 2008.
- 1195 Ye, H. C., Cho, H. R., and Gustafson, P. E.: The changes in Russian winter snow accumulation during 1936-83 and its spatial patterns, *Journal of Climate*, 11, 856-863, 10.1175/1520-0442(1998)011<0856:Tcirws>2.0.Co;2, 1998.
- Zielinski, G. A., Mayewski, P. A., Meeker, L. D., Whitlow, S., Twickler, M. S., Morrison, M., Meese, D. A., Gow, A. J., and Alley, R. B.: Record of Volcanism Since 7000 B.C. from the GISP2 Greenland Ice Core and Implications for the Volcano-Climate System, *Science*, 264, 948-952, 10.1126/science.264.5161.948, 1994.